Towards Cavity-Enhanced 2DIR Spectroscopy

A thesis presented in partial fulfillment of the requirements for the degree of

Bachelor of Science in Physics

Neomi Ashwita Lewis

Abstract

Ultrafast spectroscopy has come far in the past few decades and enabled studies in a variety of systems. However, conventional methods in the field are typically limited to optically thick samples such as solids and liquids. In the Allison group, we have developed techniques to address this gap and study dilute gas-phase molecular beams through coupling frequency combs to enhancement cavities. In previous and ongoing work, we have demonstrated the viability of this technique for transient absorption spectroscopy (TAS) in the visible and near UV. We will extend our methods to the mid-IR (3 to 5 μm) and employ them to perform two-dimensional infrared (2DIR) spectroscopy. With this development, we propose studying intramolecular vibrational redistribution (IVR) and hydrogen bonded clusters, among other systems of interest.

In this thesis, I have planned for several aspects of the cavity-enhanced 2DIR spectroscopy experiment. First, I designed a full computer-aided design (CAD) including all free-space optics and required components starting from the optical parametric amplifiers (OPAs) we will use to generate mid-IR light to the cavities themselves. Then, I simulated pressure conditions for a water clusters experiment to help inform future experimental build considerations. Finally, I completed several steps in fiber laser development for assembling one of the signal branches for difference frequency generation (DFG) in the OPAs.

Stony Brook
University

Department of Physics
Under the supervision of Prof. Thomas K. Allison
Stony Brook University
May 2021

Contents

Acknowledgments

Naturally, this work would not be possible without the guidance and scientific direction of my advisor, Prof. Allison. As almost anyone who interacts with him knows, Tom has an infectious energy to him. He is always willing to engage with details and has done a considerable amount to challenge me in my abilities. He also pushed for me to have work I could feel motivated by for this thesis. Thank you, Tom, for giving me a chance as a freshman and letting me stick around.

Much of my experience in the Allison group has been formed by Myles Silfies. He taught me much of what I know about CE-TAS, and has always helped me decipher what is going on. Myles was a great person to work with, both for his personality and his breadth of knowledge. He is also a kind and empathetic mentor and colleague, which I value. In terms of this thesis, Myles provided a lot of guidance for my work in Section 2 and worked very closely with me on the fiber laser development documented in Section 4.

Thank you, Grzegorz Kowzan, for helping me understand a lot of the basics of absorption coefficients and navigating the terminology of the various ways to represent the same thing. After some back and forth with him, I finally understood key aspects of the background in Section 3. I would also like to thank Jay Rutledge for his helpfulness. Almost every time I asked Jay for help with something, I'd get a few paragraphs of explanation in response! Thank you also to all other members of our group for their general willingness to help and company.

Finally, to two of my best friends: Marisa and Matt. Thank you, Marisa, for being my fellow monk. Thank you, Matt, for your patience and always doing the most to keep me sane.

1 Introduction

Spectroscopy is an essential tool for studying light matter interactions. Its applications are wide-ranging whether that be for medical imaging or food safety tests, and its usefulness for fundamental science questions remains plentiful. On the fundamental science front, developments in spectroscopic techniques push the frontiers of what we are able to "see" or record. In terms of how fast we can "see" phenomena, the past few decades have seen a burgeoning in the ultrafast sciences, or the ability to record signals on the femtosecond (10^{-15}) timescale. Ultrafast techniques allow us to image the incredibly fast dynamics that occur in atoms, molecules and solids when they are optically excited.

A basic model for ultrafast spectroscopy techniques is that of the pump-probe technique. In the pump-probe method, a pump pulse generates some kind of excitation in the sample. The probe pulse then 'pokes' at the excitation to determine the pump pulse's effect. The time delay between the two pulses can be varied to build an image of the evolution of the induced excitation (or polarization) [1].

1.1 Cavity-Enhanced Spectroscopy with Frequency Combs

In some ways, our work on cavity-enhanced transient absorption spectroscopy (CE-TAS) can be regarded as the marriage of ultrafast spectroscopy and cavity-enhanced direct frequency comb spectroscopy (CE-DFCS).

In the time domain, a frequency comb is a coherent train of regularly separated pulses. In the frequency domain, a comb is a set of evenly spaced frequencies. They were originally developed for frequency metrology and allowed one to measure very large frequency differences (between the optical and microwave regimes) with high precision. Frequency combs rapidly became useful for spectroscopy with a technique called direct frequency comb spectroscopy (DFCS). In this technique, a comb is used as a broadband source that interacts with an absorbing sample, and the relevant information is found in the transmission spectrum [2].

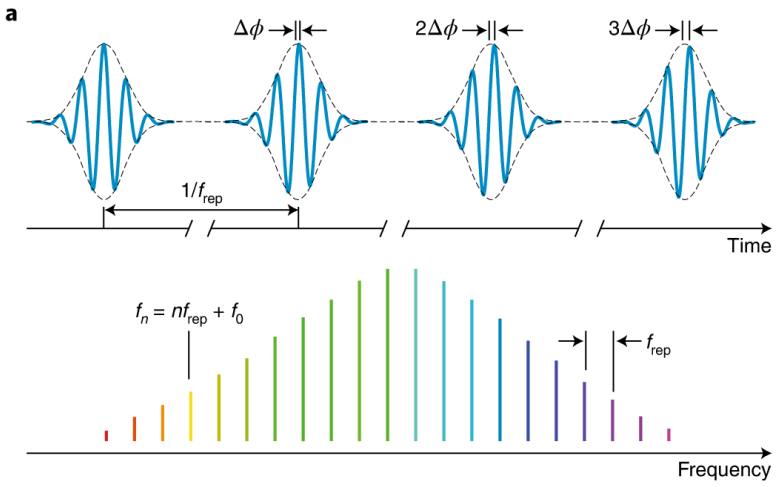

Figure 1.1: A representation of frequency combs in the time and frequency domain. In the time domain, pulses are separated by $\frac{1}{f_{rep}}$ where f_{rep} is the repetition rate of the laser. $\Delta\phi$ is the phase offset between the carrier and envelope pulse, and is directly related to f_0 in the frequency domain. While $\Delta\phi$ is time dependent, the change in $\Delta\phi$ from pulse to pulse, $\Delta\Delta\phi$, is equal to $2\pi f_0/f_{rep}$. In the frequency domain, a frequency comb laser looks like finely spaced frequencies, like the teeth of a comb. The equation $\nu_n = nf_{rep} + f_0$ describes the relationship between ν_n, the center frequency of each comb tooth, n an integer, f_{rep} the frequency separation between the teeth, and f_0 an offset frequency. Figure taken from Ref. [2].

DFCS techniques offer the large bandwidth offered by frequency combs with the resolution determined by the width of an individual 'tooth.' CE-DFCS is an enhancement of the DFCS technique in that the use of an optical enhancement cavity effectively increases the interaction length with the sample [3]. For cavity-enhanced comb techniques, naturally, one must couple the comb to the cavity. One way to understand this coupling is to view it as a time based matching where the time taken for pulses to circulate in the cavity must equal $\frac{1}{f_{rep}}$. Additionally, the carrier-envelope shift acquired by pulses in each round trip in the cavity must match the phase shift between pulses, $\Delta\phi$. This way, pulses coherently constructively interfere with each other. An alternative way to view this coupling is through considering the frequency domain, where the cavity's free spectral range must match the spacing between frequency comb teeth (or vice versa). Additionally, the cavity's f_0 must match that of the laser [4].

In CE-TAS, we essentially perform a TAS experiment with the same cavity enhancement ideas of CE-DFCS. As described in Ref. [5], the sample is excited every round trip and the signal enhancement is similar in nature to that in CE-DFCS. However, there are some important differences and challenges to CE-TAS; these are discussed in detail in Refs. [4] and [5]. These techniques

allow us to perform TAS experiments on molecular beams and other ultra-dilute samples due to the signal enhancement afforded by enhancement cavities.

The initial demonstration experiment described in Ref. [5] was only done at a single frequency, and so after considerable innovation, we now have a broadband spectrometer which has been used to study excited-state intramolecular proton transfer [6]. This work also incorporates significant technology development in building widely tunable, low noise, high-power frequency combs [4], [7] and the enhancement of those combs in a femtosecond enhancement cavity [8].

1.2 2DIR Spectroscopy

We propose extending our spectrometer and ability to perform cavity-enhanced spectroscopy to 2D spectroscopy. In 2D spectroscopy, one obtains a spectrum that is a function of both the pump and the probe wavelengths, so the two dimensions here are the two separate wavelengths. By using different wavelengths to pump and probe the sample, one determines the coupling between the two interactions related to those wavelengths. For example, if we pump at a certain frequency and then probe at another frequency and then observe no change in the spectrum, this tells us that there is no interaction between the two transitions associated with the two wavelengths.

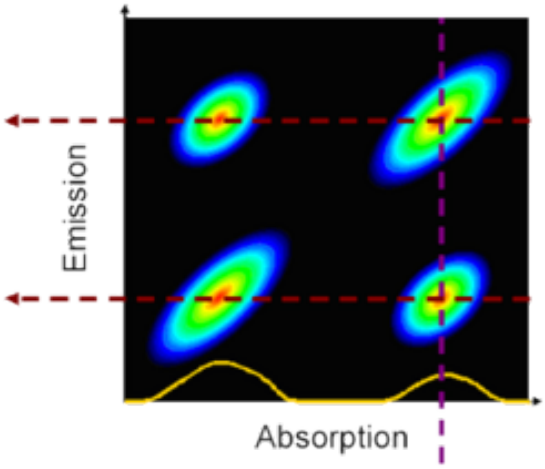

Figure 1.2: An illustration of a 2D spectrum. Important features of note include the difference between the diagonal and off-diagonal peaks. Diagonal peaks occur from pumping and probing at the same wavelength. Off-diagonal peaks occur from pumping and probing at different wavelengths so they reflect how pumping one feature affects another. Figure taken from Ref. [9].

2D spectroscopy is widely hailed as a powerful tool to record information about structure and

molecular dynamics. It also has an intrinsic ability to resolve very fast dynamics. Its applications are wide-ranging spanning from studying protein structures, to photosynthesis to materials for batteries [10].

Our realization of ultrafast 2DIR spectroscopy will be applied towards jet-cooled molecules and elucidate much about their dynamics that is currently difficult to observe with linear spectroscopy. Two particular problems of interest are that of intramolecular vibrational redistribution (IVR) and hydrogen-bonded clusters.

IVR is the process through which vibrational energy is redistributed in a system [11]. That is, after some initial excitation and local motion, a polyatomic molecule or collection of molecules will find itself in a different vibrational state than the one it started off in. IVR describes a fundamental step in understanding rates in chemical reactions. An understanding of how IVR occurs, even in simple systems, has proven to be difficult to pinpoint. Studies of IVR are also attractive because they suggest the possibility of control over chemical reactions.

There is also much that is not yet understood about the hydrogen bond, and we propose studying it in clusters as a way of studying a simple hydrogen-bonded system. The hydrogen bond is both similar to weaker interactions and more robust bonds, so the definition of the 'bond' remains unclear. For example, it gives DNA/RNA structure but is weak enough that these structures can unzip and replicate themselves when needed. It also determines the unique properties of water like its anomalous boiling point, where it has a high boiling point for its molecular weight and does not follow the trend other polar molecules do, which contribute to its role as nature's most important solvent. One characteristic of the hydrogen bond that makes it difficult to study or simulate is its high cooperativity. In a hydrogen-bonded system, each bond can strengthen and weaken the systems of bonds around it in a non-trivial way [12]. In the proposed CE-2DIR experiment of hydrogen-bonded water clusters, we will study clusters of varying sizes while probing the effect of exciting bonds on surrounding bonds in the network.

1.3 Non-Linear Fiber Optics

The fiber laser developments proposed for the CE-2DIR experiment and discussed in Sec. 4 rely on a combination of non-linear optical phenomena. Ultimately, the frequency-shifting that will be employed to achieve tunability of the mid-IR combs depends on these too, particularly in fiber

optics. An implementation similar to our scheme is discussed in Ref. [13].

First, briefly, non-linear optical phenomena can be described by the non-linear dependence of induced polarizations on the electric fields that cause them. This non-linear dependence effectively changes the properties of the medium and leads to a host of different phenomena [14]. In the linear regime, the induced polarization, $\tilde{P}(t)$ depends on the electric field, $\tilde{E}(t)$ in the following way:

$$\tilde{P}(t) \approx \epsilon_0 \chi^{(1)} \tilde{E}(t) \tag{1.1}$$

Here, ϵ_0 is the permittivity of free space, $\tilde{E}(t)$ the electric field interacting with the medium and $\chi^{(1)}$ the linear susceptibility, a factor that relates $\tilde{P}(t)$ and $\tilde{E}(t)$.

In the non-linear regime, we can express $\tilde{P}(t)$ as a power series in $\tilde{E}(t)$ as follows

$$\tilde{P(t)} = \epsilon_0 \left[\chi^{(1)} \tilde{E}(t) + \chi^{(2)} \tilde{E}^2(t) + \chi^{(3)} \tilde{E}^3(t) + ... \right] \tag{1.2}$$

As shown in Eq. 1.2, in considering non-linearities, the induced polarization no longer depends just linearly on the incident field but can depend on the field squared, or cubed, or to the fourth power etc.

Many non-linear effects in fibers, for example, can be described by $\chi^{(3)}$, the third-order susceptibility. (Most fibers also do not have a $\chi^{(2)}$ as glass has inversion symmetry [15].) For example, the spectral broadening that we will need for the signal branch occurs through a phenomenon that $\chi^{(3)}$ describes (four-wave mixing) [16]. More generally, nonlinear refraction depends on $\chi^{(3)}$. This phenomenon describes the dependence of the refractive index, $\tilde{n}(\omega)$, on the intensity of the incident field, $|E|^2$. That is,

$$\tilde{n}(\omega, |E|^2) = n(\omega) + n_2 |E|^2 \tag{1.3}$$

Here, n_2 is the non-linear index coefficient, related to $\chi^{(3)}$ in the following way,

$$n_2 = \frac{3}{8n} \mathrm{Re} \left[\chi^{(3)}_{xxxx} \right] \tag{1.4}$$

Here, $\chi^{(3)}_{xxxx}$ is a component of the fourth-rank $\chi^{(3)}$ tensor; only one element is included in the

definition in Eq. 1.4 as the light is assumed to be linearly polarized.

Non-linear refraction is responsible for self-phase modulation (SPM); this is a phenomenon in which a propagating pulse induces a phase shift on itself. This can be seen through considering the phase induced by Eq. 1.3, ϕ:

$$\phi = \tilde{n}kL = nkL + n_2|E|^2kL \tag{1.5}$$

Here, k is the wavenumber of the propagating pulse and L the length of the propagating medium/fiber. The second term in the equation above corresponds to some non-linear phase shift, $\phi_{NL} = n_2|E|^2kL$, which is attributed to SPM. Note again that ϕ_{NL} depends on the intensity of the field. Further, if one considers the instantaneous frequency, $\omega(t)$,

$$\omega(t) = \frac{d\phi}{dt} = n_2kL\frac{dI}{dt} \tag{1.6}$$

Here, $I = |E|^2$ is the intensity of the incident field. The relation in Eq. 1.6 can result in the generation of new frequencies depending on $\frac{dI}{dt}$. For example, for an incident Gaussian pulse, SPM broadens the pulse symmetrically, shifting the red portion of the pulse to longer wavelengths and the blue portion to shorter wavelengths.

There are other non-linear effects beyond the effects of $\chi^{(3)}$ that become relevant for the propagation of ultrashort pulses in fiber. An example of this is stimulated Raman scattering (SRS), where a part of the propagating pulse's energy is lost to the medium in the inelastic process of Raman scattering. The process here is stimulated by the incoming light acting as a pump. This pump light is scattered off the medium, losing energy, while the medium's molecules gain energy and transition to higher vibrational states. The scattered light forms what is called a "Stokes wave". In a non-linear medium, the Stokes wave can grow so quickly that most of the pump energy is depleted inside the medium [15].

It is also important for us to consider linear dispersion in our consideration of the propagation of pulses. That is, the $n(\omega)$ of Eq. 1.3 also depends on the wavelength of light. We can consider this chromatic dispersion through expanding $\beta\left(= n(\omega)\frac{\omega}{c}\right)$, the propagation constant, as a Taylor series around the center frequency of a given spectrum, ω_0 [15],

$$\beta = \beta_0 + \beta_1(\omega - \omega_0) + \frac{1}{2}\beta_2(\omega - \omega_0)^2... \tag{1.7}$$

The different terms in Eq. 1.7 can be related to different terms relevant to pulse propagation. For example,

$$\beta_1 = \frac{1}{v_g} \tag{1.8}$$

where v_g is the group velocity, i.e. the velocity at which the pulse envelope travels. As $\beta_2 = \frac{d\beta_1}{d\omega}$, β_2 describes the dispersion of the group velocity or pulse broadening. For this reason, β_2 is also known as the group velocity dispersion (GVD) parameter. β_2 is related to another commonly used parameter, D $= \frac{d\beta_1}{d\lambda}$, in the following way:

$$\beta_2 = -D\frac{\lambda^2}{2\pi c} \tag{1.9}$$

Chromatic dispersion also results in linear chirp wherein the instantaneous frequency of the light changes with time. This is called a 'chirp' because dispersion's frequency dependence means different frequencies travel at different speeds, and the effect mimics what we perceive when hearing a bird's chirp (i.e. that higher or lower frequencies of a bird chirp are heard first). A positive chirp is defined by GVD > 0, and lower frequencies travelling faster. A negative chirp is defined by GVD < 0, and higher frequencies travelling faster.

A combination of the effects discussed above and others not mentioned here lead to the host of pulse propagation effects that describe the effects we utilize for our experiments. For example, the formation of solitons, pulses that travel with constant temporal and spectral shape, results from a balance of SPM and chromatic dispersion. Soliton formation is important for the broadening effects we require to generate broad spectra for the signal branch [16].

1.4 Proposed Build

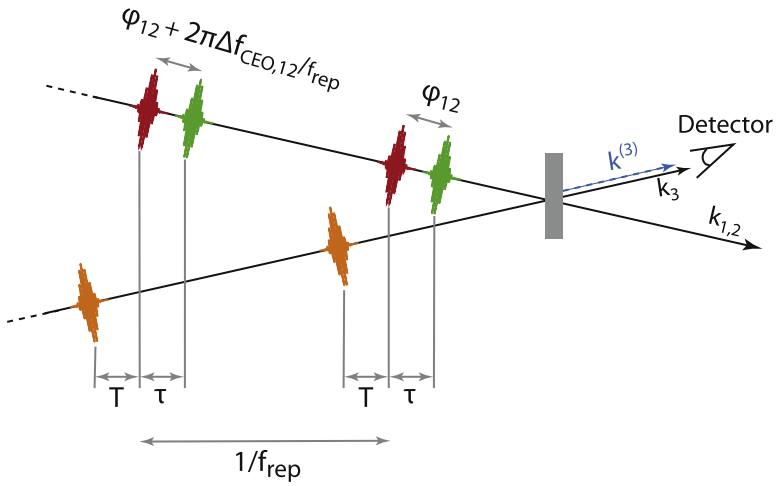

Figure 1.3: A schematic of the 2DIR experiment, with the two offset pump pulses shown in maroon and green and the probe pulses shown in orange. The time delay between pump pulse is labelled as τ, and the time delay between the second pump and probe pulse as T. Figure taken from Ref. [17].

The cavity-enhanced 2DIR spectrometer will operate between the 3 to 5 μm range, and will use two tunable mid-IR combs. We will couple these two combs into two cavities – one for the pump beams and one for the probe beam. The two pump combs for 2DIR will be offset by $f_{\text{rep}}/2$ to record purely absorptive 2DIR spectra [17]. This frequency shift will be achieved by diffracting one of the beams off a free-space acousto-optical modulator (AOM). More details on this phase cycling scheme are available in Sec. 2.2 and Ref. [17].

To generate these mid-IR combs, we will use near-IR combs derived from a 100 MHz Er:fiber comb for difference frequency generation (DFG). The scheme for this experiment is very similar to the first stage of an existing optical parameter amplifier (OPA) scheme in our group which is described in Ref. [18].

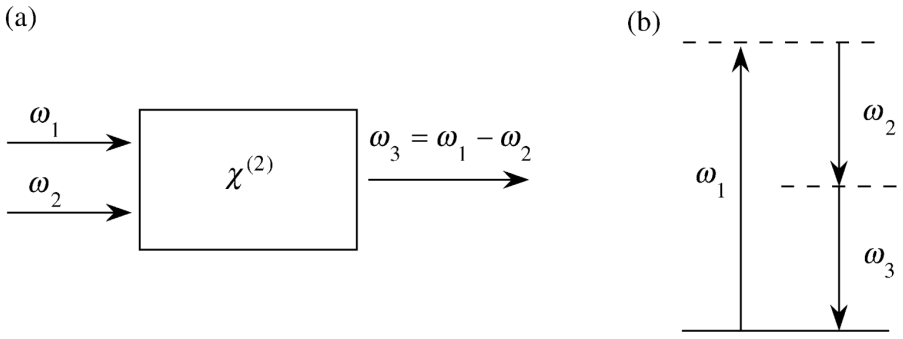

Figure 1.4: A simple schematic illustrating DFG. Fig. (a) demonstrates the non-linear process as a phenomena in which one generates light with an frequency that is the difference of the two incoming frequencies. Fig. (b) represents this process with energy levels. More information on the non-linear physics occurring during DFG is available in Ref. [14]. In discussing DFG and the OPAs in this work, I refer to ω_1 as the pump, ω_2 as the signal and ω_3 as the idler. For this experiment, our pump wavelength is 1.06 µm and our signal wavelength will be tunable between around 1.3 to 1.7 µm. This results in an idler tunable from 3 to 5 µm. DFG will occur in a 5%-MgO-doped periodically poled lithium niobate (PPLN) crystal as was used in the work in Ref. [18]. Figure taken from Ref. [14].

Important distinctions from the work in Ref. [18] is the need for tunable carrier-envelope offset frequency (f_0) and general tunability for the mid-IR light. The first is required because the cavity's f_0 varies with idler wavelength so we must be able to match these changes to maintain coupling. This will be achieved with fiber-coupled AOMs in the signal branches to tune the signal f_0s. The second distinction will be achieved by changing the power in the highly non-linear fiber (HNLF) used for supercontinuum generation (see Sec. 4), in a similar way to the work in Ref. [13]. More details on the derivation of these combs and the fiber laser development required for them is available in Sec. 4.

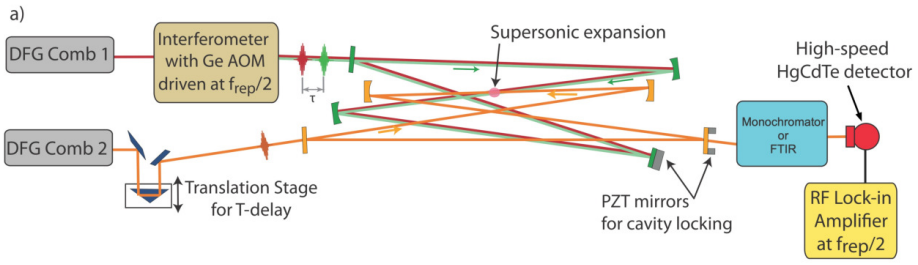

Figure 1.5: An illustration of the experimental setup. Twin OPAs (one for the pump, one for the probe) are a part of the DFG Combs labelled here. Then, we will use an AOM in the pump's path to make two offset pump combs. More details are discussed in the text below.

Signals will then be recorded with either a monochromator or FTIR interferometer with a high-speed mid-IR detector as shown in Fig. 1.5. The time delays between pulses will be controlled with mechanical stages, as shown in Fig. 2.2. The normalized molecular signal will be retrieved with lock-in detection utilizing modulation on the probe beam at $f_{\mathrm{rep}}/2$ [6].

Thesis Outline

In this work, I have planned for several aspects of the CE-2DIR experiment detailed above. In Chapter 2, I consider the various free-space optics needed for the experiment from our shifted frequency combs to the cavities, and detail a CAD design for this aspect of the experiment. In Chapter 3, I consider how different pressures affect measurement conditions in a water clusters experiment. In Chapter 4, I return to the problem of generating mid-IR light through considering the fiber laser development required for the signal branch leading up to the OPAs.

2 CAD Modelling

In this chapter, I detail a plan for all free-space components needed for the 2DIR experiment leading up to and including the cavities. The planning of this blueprint was partly motivated by the desire to find a space-efficient layout including all equipment that is needed. This process involved considering what lenses the OPAs need, the use of an AOM (acousto-optical modulator) for using specific spatial modes in the cavity and cavity design itself.

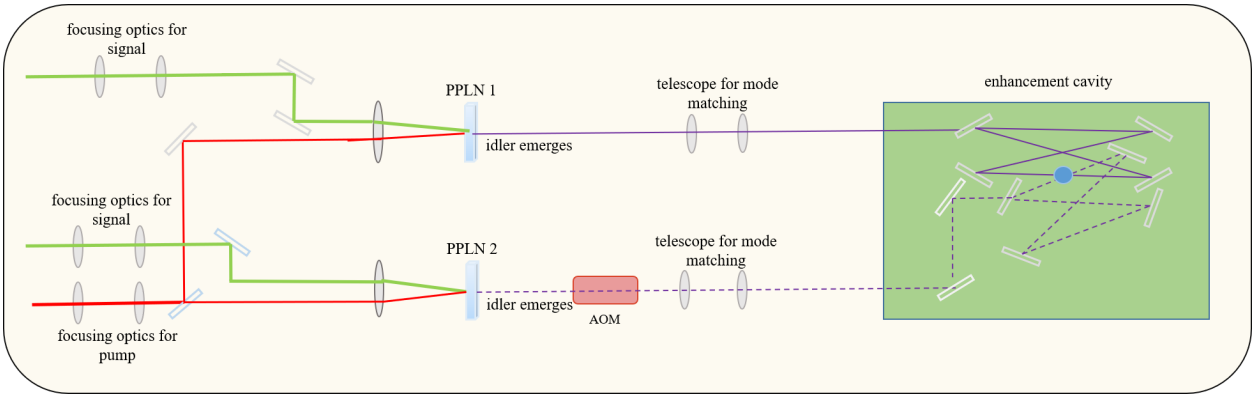

Figure 2.1: A simplified schematic of the free-space elements considered and the twin OPAs. The green beams are the signal, the red the pump and the purple beams the two idler beams. The pump will be at 1.06 µm, the signal tunable between 1.3 to 1.7 µm to give a tunable idler between 3 to 5 µm. DFG occurs in the two PPLN crystals labelled PPLN 1 and PPLN 2. One set of these idler beams will act as the pump for the experiment, and another as the probe. The pump set will be separated into two beams, one of which will have its f_0 shifted with a free space AOM for a phase cycling scheme (more details in chapter). The pumps and probe are coupled into the enhancement cavity in green where the molecular jet's position is denoted by the blue circle.

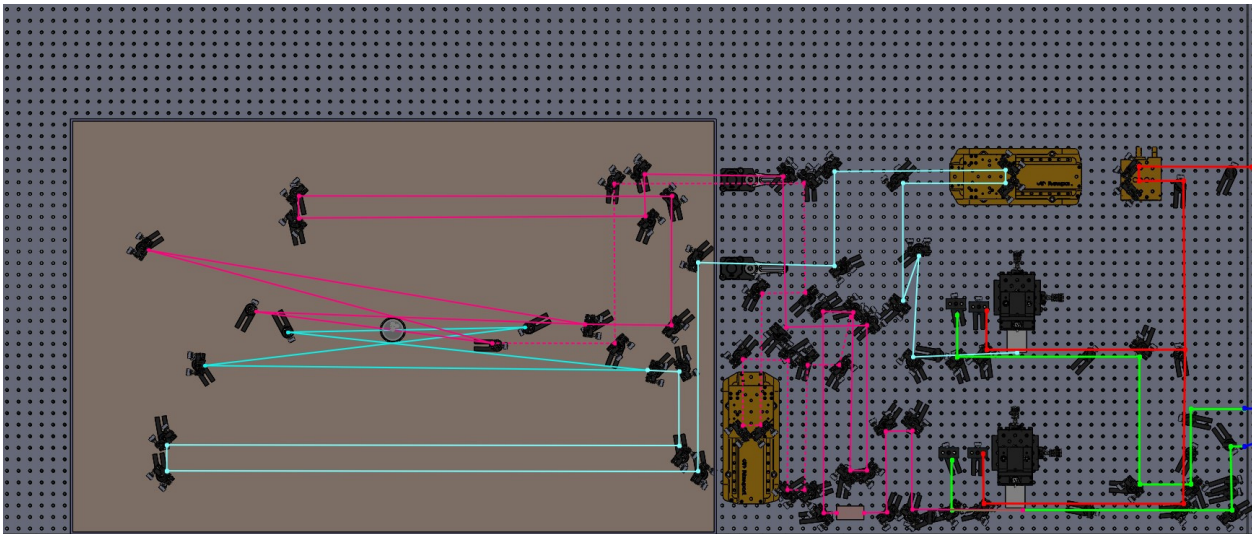

Figure 2.2: A bird's eye view of the full CAD model. The grid of holes on the table have 1" spacing. Each section of the model is explained and detailed in consequent sections of the text below.

2.1 Lens Considerations for OPAs

In order to have efficient difference frequency generation (DFG) at the PPLN crystal, our pump beam must be focused to a spot size such that the incident pump intensity on the crystal is between 5 to 10 GW/cm^2. Exceeding 10 GW/cm^2, however, would damage the crystal [19]. In general, one can achieve good DFG efficiency and idler beam quality in an OPA when the pump and signal beams have the same size [20]. The relationship between beam parameters and efficient DFG can be considered in more detail during the OPA build. These two facts (of the damage threshold and matching beam sizes) effectively pose the first constraints on lens choices for the pump and signal branches.

Assuming a pump power of 5 W with a 100 MHz pulse repetition rate, each pulse has about 50 nJ of energy. Our pulse duration is 100 fs.

The peak power of each pulse is then

$$P_{peak} = \frac{\text{energy}}{\text{time}} = \frac{50\text{nJ}}{100\text{fs}} = 0.5\text{MW} \tag{2.1}$$

Using the equation for a Gaussian beam [21], we can also calculate the peak intensity from

$$I_{peak} = \frac{2P_{peak}}{\pi\omega^2} \tag{2.2}$$

where ω is the radius of the Gaussian beam.

Rearranging Eq. 2.2, and using the peak power of Eq. 2.1, we find that a waist of 56 μm will give us a peak intensity of 10 GW/cm^2 at the crystal. This provides an estimate for a target waist to focus to.

Gaussian Beams and ABCD Matrices

I modeled the effect of different lenses on my beam parameters using ABCD parameters. First, recall that Gaussian beams can be described by their so-called complex beam parameter, q [22]. q is defined as

$$\frac{1}{q} = \frac{1}{R} - i\frac{\lambda}{\pi\omega^2} \tag{2.3}$$

Here, R is the radius of curvature of the beam, λ the wavelength of light and ω the beam size.

We can describe how the beam size, ω, changes with ABCD matrices. For a given ABCD matrix, the complex beam parameter q' after the elements in the matrix is

$$q' = \frac{Aq_0 + B}{Cq_0 + D} \tag{2.4}$$

where q_0 is the initial q.

So, for lens arrangements considered, I found how the particular arrangement changed q using Eq. 2.4. I then retreived the beam size, ω, from q by taking its imaginary part (see Eq. 2.3).

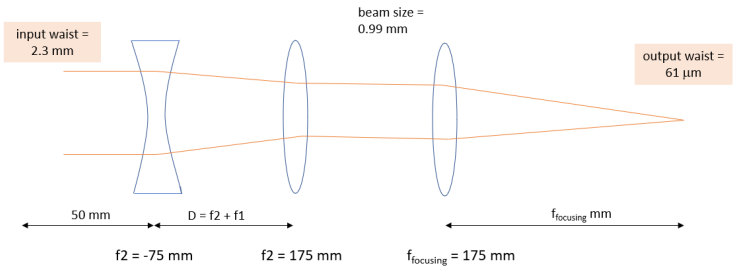

Figure 2.3: Lens configuration used for pump. Here lenses 1 and 2 form a telescope that decreases the beam size, before it is focused by a focusing lens. This focusing lens will be the same one used by the signal, and focuses the pump at 1060 nm to a 61 μm spot size.

Chromatic Aberration

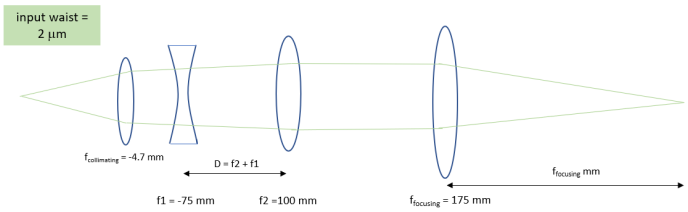

Figure 2.4: Lens configuration used for signal. The input waist is assumed to be 2 μm, based on the fact the HNLF the signal will be launched from has a mode field diameter of approximately 4 μm [23]. Here lenses 1 and 2 form a telescope that expands the beam size, before it is focused by a focusing lens. This focusing lens will be the same one used by the pump, and focuses the signal to a spot size of approximately 58 μm. The actual spot size depends on the the wavelength of the signal. Focal length labels are nominal.

As the signal wavelength is a range of wavelengths (from approximately 1.3 to 1.7 µm) instead of one discrete wavelength like the pump, it is relevant to consider how chromatic aberration affects lensing and focusing properties.

In my consideration of chromatic aberration, I calculated the index of refraction for each wavelength of consideration using the Sellmeier formula for the refractive index, n, of fused silica, Eq. 2.5 below [24].

$$n(\lambda)^2 - 1 = \frac{0.6961663\lambda^2}{\lambda^2 - 0.0684043^2} + \frac{0.4079426\lambda^2}{\lambda^2 - 0.1162414^2} + \frac{0.8974794\lambda^2}{\lambda^2 - 9.896161^2} \tag{2.5}$$

Recall that the focal length of a lens, f, is given by [25]:

$$\frac{1}{f(\lambda)} = (n(\lambda) - 1)\left(\frac{1}{R_1} - \frac{1}{R_2}\right) \tag{2.6}$$

Here, n is the refractive index of the lens and R_1 and R_2 the radii of curvature of the two faces of the lens.

In this case, as I used plano-convex and plano-concave lenses, Eq. 2.6 becomes

$$\frac{1}{f(\lambda)} = (n(\lambda) - 1)\frac{1}{R} \tag{2.7}$$

Here, R is the radius of curvature of the curved face of the lens.

After some considerations on the effect of chromatic aberration on the focal length of lenses, i.e. the fact that the the refractive index in Eq. 2.5 depends on wavelength, in final calculations, I only considered the effect of chromatic aberration on the collimating and focusing lenses. This was based on the observation that in modelling chromatic aberration on the entire setup of lenses, the lenses that most strongly determined shifts in focus position/size were the collimating and focusing lenses.

Calculations on the position of the minimum beam size/waist size when accounting for the chromatic aberration in the collimating and focusing lens are shown in Fig. 2.5. Fig. 2.6, on the other hand, shows the results of the calculation on the size of the waist.

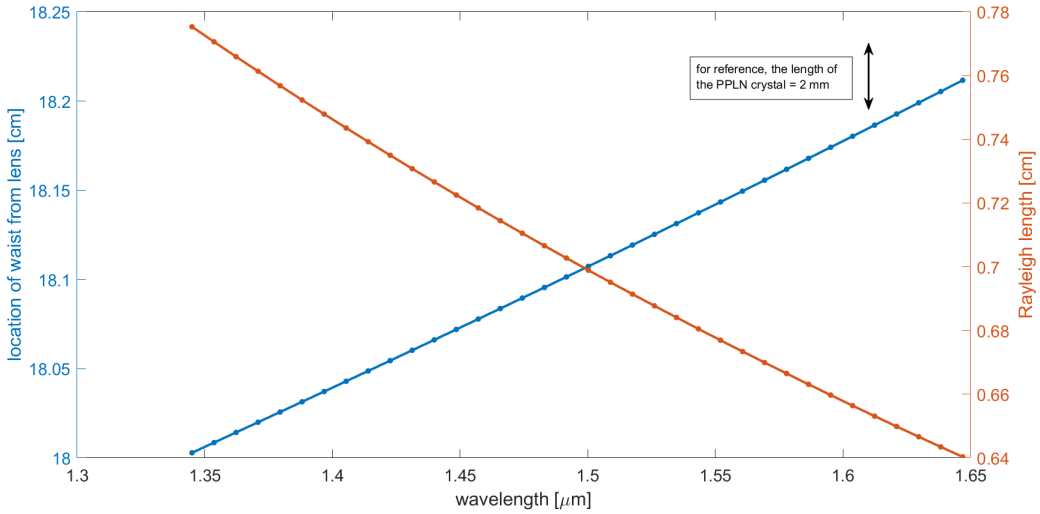

Figure 2.5: Location of waist and Rayleigh length, z_R, vs. wavelength. The left y-axis here denotes distance from the focusing lens, not from the input beam. There is a 1.4 mm shift in the position of the focus. While this shift on its own is not surprising, it becomes more relevant in considering where exactly to place the crystal relative to the focusing lens. Further, the Rayleigh length changes occur on a slower rate. Importantly, the focus shift is small compared to the confocal parameters ($2z_R$), such that the beam is still effectively "in focus" at the PPLN. This sets a scale along which the position of the crystal can be varied.

Another metric for how bad this chromatic aberration is to judge how much the waist varies for different wavelengths when the crystal is placed at a fixed location. This, of course, determines how much the signal waist will change at different wavelengths and informs the efficiency/quality of DFG. In Fig. 2.6, I place the crystal at the focal length for the center wavelength in the signal wavelength range. At this location, the waist size (or spot size) does not vary dramatically. Shifting

from this location by 1 mm, shown in Fig. 2.7, naturally makes waist size variation larger but only about 0.5 µm. However, if one moves the crystal even further, say, by 3 mm, as shown in Fig. 2.8, the variation in waist size increases to about 9 µm from the best case scenario of 1 µm. From these calculations, we can conclude that as long as one keeps the distance between the focusing lens and PPLN crystal close (a few mm) to the center focal length, variation in waist size will stay small and one does not need to worry about chromatic aberration. From another perspective, the variation of the waist along the length of the crystal (2 mm) will not pose significant chromatic aberration issues.

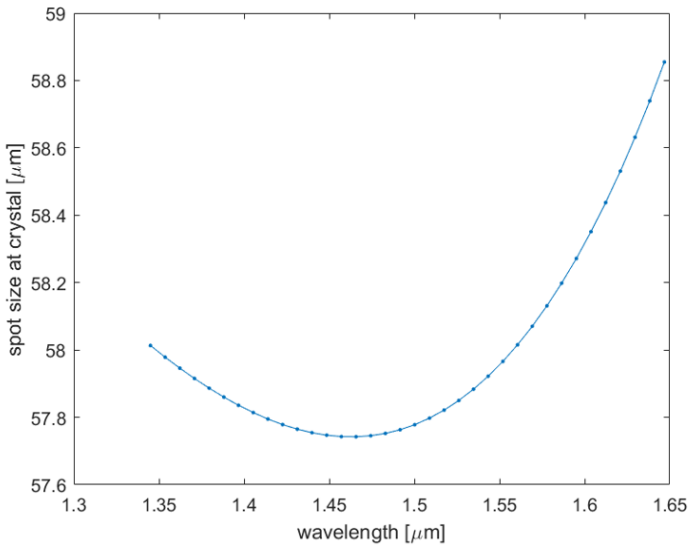

Figure 2.6: If the crystal is placed in the center of the range in Fig. 2.5 = 18.1 cm, the variation in spot size is small, ranging from approximately 57.7 to 58.8 μm.

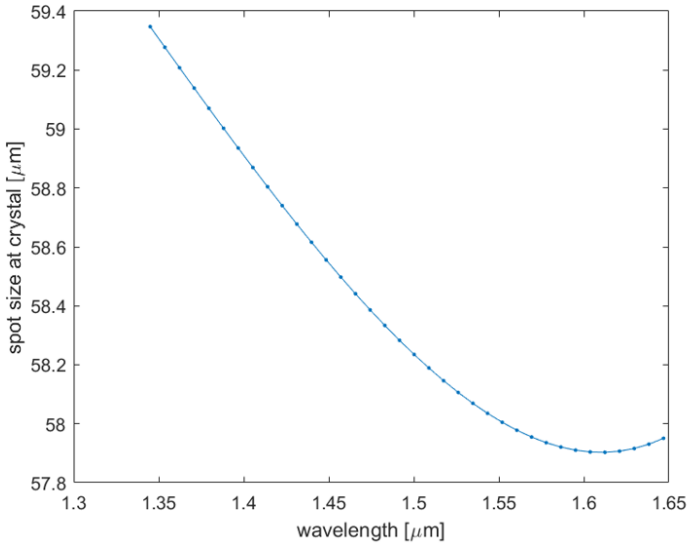

Figure 2.7: If the crystal is shifted by 1 mm from the center focal length (distance from focusing lens = 18.2 mm), the variation in spot size is remains small but increases to approximately 1.5 μm from the 1 μm variation in Fig. 2.6. The spot sizes are also larger as we are more off from optimal focal lengths for all wavelengths; this could be utilized to have the signal spot size more closely match the pump's spot size.

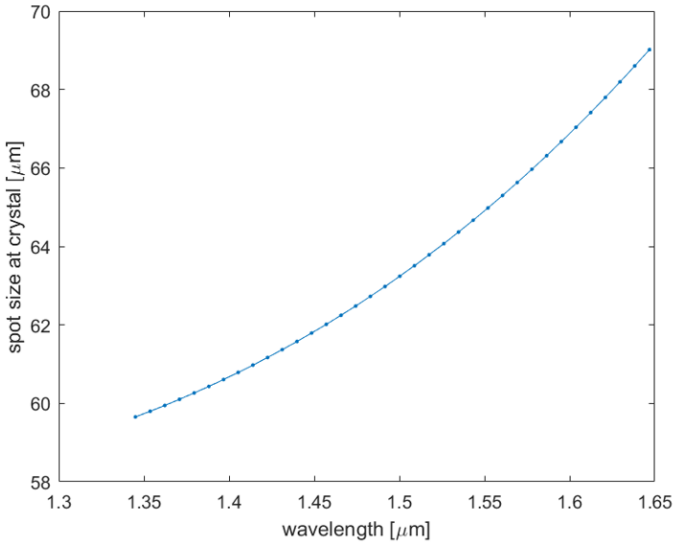

Figure 2.8: If the crystal is shifted by 3 mm from the center focal length (distance from focusing lens = 17.8 mm), the variation in spot size is much larger, ranging in about 9 μm.

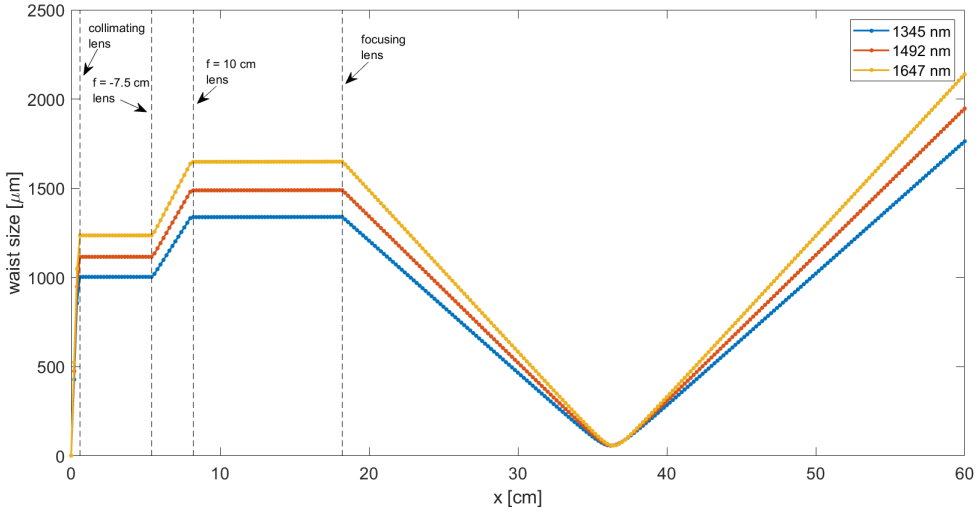

Figure 2.9: Finally, a consideration of how beam sizes change for different signal wavelengths across the entire arrangement in Fig. 2.4. x is the distance from the input in cm. The vertical dashed lines show the positions of the different lenses in the arrangement; the first horizontal section reflects collimation from the collimating lens, and the second collimation from the telescope (f = -7.5 cm and f = 10 cm lenses). Then, we see all beams being sharply focusing by the focusing lens to a focus around 37 cm from the input.

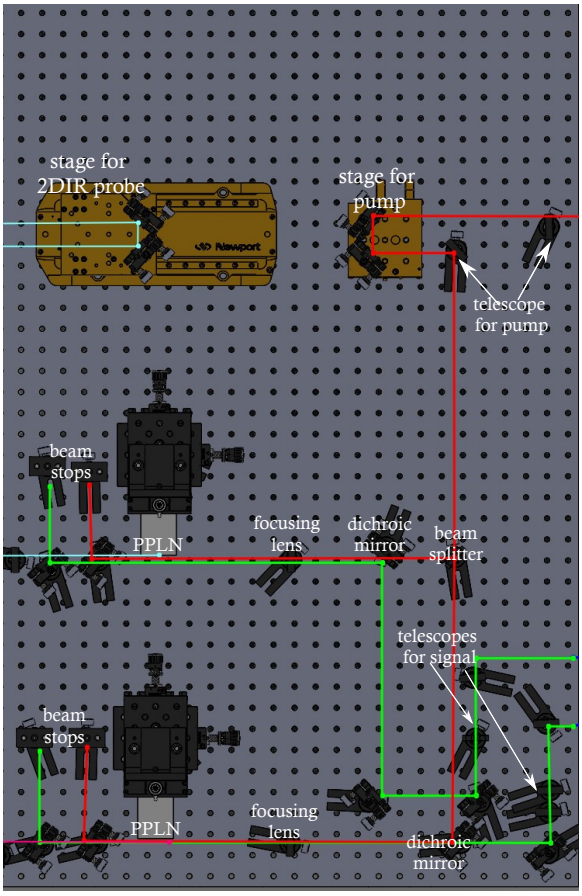

Figure 2.10: The configuration of optics and lenses used for the full CAD model of Fig. 2.2. Here, the pump for DFG is shown in red and the signal in green. Dichroic mirrors are used along the paths of the beams being combined at the PPLN for DFG. After the PPLN, the signal and pump are dumped on beam stops and the idler used for the experiment.

	$f_{collimating}$ [mm]	f_1 [cm]	f_2 [cm]	$f_{focusing}$ [cm]	waist at crystal [μm]
pump	N/A	17.5	-7.5	17.5	61
signal	4.7	-7.5	10	17.5	58 (approx)

Table 2.1: A summary of the lenses chosen, with the corresponding spot sizes achieved

2.2 Phase Cycling Scheme

In the proposed experiment, three pulses are used to induce a nonlinear polarization in the sample. The first two pulses are the pump pulses and the third the probe pulse. We can describe the induced nonlinear polarization, $P^{(3)}$, as the following [26]:

$$P^{(3)}(\vec{r},t) \propto \int_0^\infty dt_3 \int_0^\infty dt_2 \int_0^\infty dt_1 \sum_n R_n(t_1,t_2,t_3) E_3(\vec{r},t-t_3) E_2(\vec{r},t-t_3-t_2) E_1(\vec{r},t-t_3-t_2-t_1) \tag{2.8}$$

Here E_1 is the field of the first pump pulse that interacts with the system, E_2 the field of the second pump pulse and E_3 the field of the probe pulse. t_1 is the delay between E_1 and E_2, t_2 the delay between E_2 and E_3, and t_3 the delay between E_3 and the emitted field. R_n is the third-order system response terms that result from this non-linear interaction.

Now, in general, if one considers all possible pathways that are described in Eq. 2.8, the induced polarization and emitted field will be the result of many different types of interactions. More details on this can be found in Ref. [26]. One may instead want to isolate a particular kind of response. For example, in this case, we propose detecting only absorptive signals from the molecular samples. There are several different ways spectroscopists isolate a desired response, the most common of which include only detecting the emitted signal in a particular direction, or by modulating the pulses combined with lock-in detection. Phase modulation using the latter technique is called phase cycling.

In our case, we propose achieving phase cycling by coupling offset pump frequency combs into different cavity modes, by doing so, we will record only absorptive signals. The details of this method and its implementation are discussed in Ref. [17]. Essentially, as Allison explains, one can have the f_0 offset between pump pulses exactly match the Gouy phase shifts those separate pump combs acquire by inhabiting different Hermite-Gaussian modes in the cavity. Doing so allows one to 'naturally' phase cycle the two pump combs. There are several advantages to this technique, which are again discussed in some detail in Ref. [17], one of which includes the ability to detect a background-free absorptive signal.

In terms of design considerations relevant to this work, one must have the two pump combs have the relevant f_0 shift between them to naturally phase cycle in different modes. In the case of coupling different combs to the same cavity,

$$\Delta f_0 = f_{rep} \frac{\Delta\phi}{2\pi} \tag{2.9}$$

Here, $\Delta\phi$ is related to the Gouy phase shift acquired by the two combs per round trip depending

on which spatial Hermite-Gaussian modes they occupy:

$$\Delta\phi_{12} = (l_1 - l_2)\psi_{tan} + (m_1 - m_2)\psi_{sag} \tag{2.10}$$

Here, ψ_{tan} and ψ_{sag} are the Gouy phase shifts in the tangential and sagittal planes, and depend on the geometry of the cavity [17]. 'l' and 'm' refer to the mode numbers of the Hermite-Gaussian modes themselves. Naturally, the two pump beams must also occupy different Hermite-Gaussian modes to have a non-zero $\Delta\phi_{12}$ (if $l_1 = l_2$ and $m_1 = m_2$, we have no Gouy phase shift between them). One possible way to change the spatial mode of one of the pump beams is to use a phase mask in its path.

Then, we need to match the pulse to pulse CE-phase difference between the beams given by their f_0 to the difference in the Gouy phases they acquire in a round trip. To introduce a f_0 shift between the pumps, we propose using a free-space acousto-optic modulator (AOM) to shift one of the pump beam's f_0 by $f_{rep}/2$. This results in a $\Delta\phi_{12} = \pi$ which is relevant for isolating absorptive signals [17] [26]. The AOM we will use is a Germanium AOM from Brimrose Corporation, with model no. GEF-45-10-2000/5000.

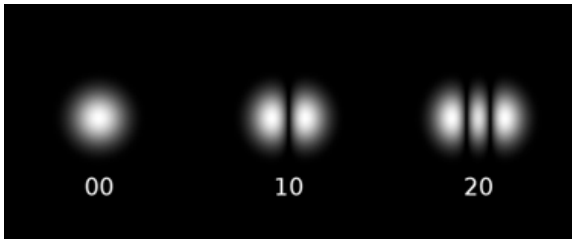

Figure 2.11: Some examples of Hermite Gaussian modes. The plan is to have the pump beams occupy the 00 mode and 20 mode (or equivalently, the 02 mode). We intend to spatially modify one of the pump beams to look more like the 20 mode by placing a phase mask in its path. Figure taken from [27].

For my CAD design, I then made sure to include an AOM in the pump beam's path. The two beams that come out of the AOM are separated by about 1.55 - 2.56°, depending on the wavelength of the pump between 3-5 μm. This angular separation between the two pump beams is twice the Bragg angle,

$$\theta_{sep} = \frac{\lambda f}{V} \tag{2.11}$$

Here, λ is the frequency of light, f the driving RF frequency $= \frac{f_{rep}}{2} = 50$ MHz and V the acoustic velocity in Germanium (5 mm/µs) [28].

Keeping this angular separation in mind, I allowed for an appropriate distance before the beams are separated. One of the beams also travels on a stage, which will be used to change the time separation between the arrival of the pump pulses, as is required for 2DIR (as shown in Fig. 1.5). I also accounted for space for a telescope and focusing optics, to allow one to ensure they do not exceed the intensity for optical damage threshold ($= 5$ W/mm^2) of the AOM.

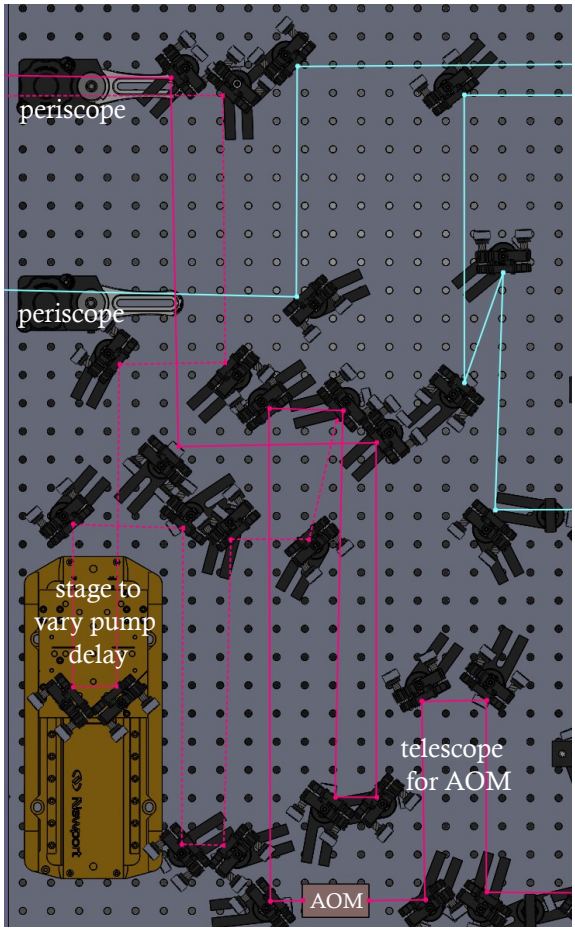

Figure 2.12: CAD for portion of setup after PPLN crystals leading up to the cavity. Here, the pumps for 2DIR is shown in pink, with the shifted pump shown with a dashed line. The cyan beam is the probe for 2DIR. One pump is also put on a long (125 mm travel) stage to introduce a time delay between the two pumps for the 2DIR experiment. The model also includes a telescope to focus into the AOM. Finally, all beams are folded in a way to allow enough space for telescopes for mode matching into the cavity to be placed in their paths. The details of these telescopes will be decided during the experiment build. The three beams enter the cavity through the periscopes in the top left.

2.3 Cavity Design

Stable Optical Cavities

In deciding the geometry of an optical cavity, one must choose parameters such that the cavity is stable and light exhibits periodic behavior within it.

One way to conceptualize stability criteria is to consider the ABCD matrix of a cavity. Beams of light that stay in the cavity will experience the elements that make up that cavity multiple times. In other words, we want the elements of the ABCD matrix of the cavity to exhibit periodic and not divergent behavior [22].

Invoking Sylvester's theorem,

$$\begin{pmatrix} A & B \\ C & D \end{pmatrix}^n = \frac{1}{\sin(\theta)} \begin{pmatrix} A\sin(n\theta) - \sin((n-1)\theta) & B\sin(n\theta) \\ C\sin(n\theta) & D\sin(n\theta) - \sin((n-1)\theta) \end{pmatrix} \tag{2.12}$$

where

$$\cos(\theta) = \frac{1}{2}(A + D) \tag{2.13}$$

In order for θ to stay real, and then have the elements of Eq. 2.12 display periodic behavior, the right hand side of Eq. 2.13 must be between -1 and 1. If θ was imaginary, the elements of Eq. 2.12 would be hyperbolic sines and cosines and the beam would deviate exponentially from the propagation axis.

It can also be shown that multiple Hermite-Gaussian modes can be resonant within the same cavity as long as the phase acquired by the different modes is equal to an integer multiple of 2π [22]. That is, the phase shift acquired by the different modes, δ, must equal $2\pi q$ where 'q' is an integer. δ is given by:

$$\begin{aligned} \delta &= \frac{\omega}{c}d + \phi_{Gouy} + \phi_{mirror} \\ &= \frac{\omega}{c}d - \frac{(n+m+1)}{2}cos^{-1} \pm \left(\sqrt{(A+D+2)/4}\right) + \phi_{mirror} \end{aligned} \tag{2.14}$$

Here, the first term in Eq. 2.14 is the phase acquired by a round-trip in a cavity of length d, the second term the Gouy phase shift with each mode where n and m refer to the mode numbers of the Hermite-Gaussian mode, and ϕ_{mirror} an additional phase shift associated with the cavity

mirror coatings. A and D are elements of the ABCD matrix that describe the cavity.

Rearranging Eq. 2.14, the resonant frequencies satisfy the following equation:

$$\nu_{nmq} = \left(q + \frac{(n+m+1)}{2} \frac{cos^{-1} \pm \left(\sqrt{(A+D+2)/4} \right)}{\pi} - \frac{\phi_{mirror}}{2\pi} \right) \frac{c}{d} \tag{2.15}$$

So, in designing cavities to be resonant for both pump beams which occupy different Hermite-Gaussian modes, one must also ensure cavity parameters satisfy Eq. 2.15. More specifically, we would want the $\Delta\nu$ determined by cavity parameters and the chosen modes to be exactly equal to the frequency shift (50 MHz) between the two pump combs. A representation of this consideration as a function of curved mirror separation is shown in Fig. 2.14.

Cavity Design Considerations

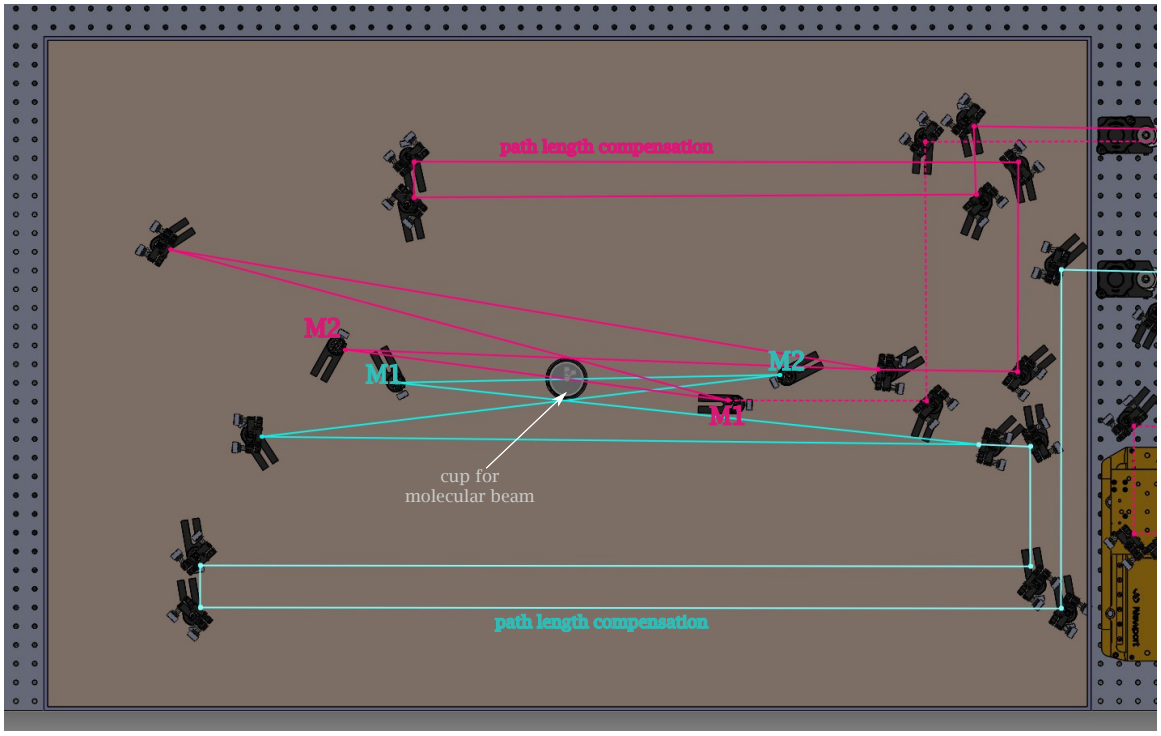

Figure 2.13: CAD of cavity design implemented. In this model, the pink lines indicate pump beams, with the dashed pink being the pump beam with a shifted f_0. The cyan beams indicate probe beams. Two paths are folded in the cavity and labelled as 'path-length compensation' as they exist to make sure all three beams have travelled the same path length from the PPLN crystal to the nozzle. Both cavities chosen are identical and have their smaller waists overlap at the center of the cup, which has diameter 2.2 inches. 'M1' indicates curved mirror 1, which has radius of curvature 40 cm and 'M2' curved mirror 2 with radius of curvature 55 cm. These are asymmetric cavities.

M1's ROC [cm]	M2's ROC [cm]	waist [μm]	distance between mirrors [cm]	distance between M1 and waist [cm]
40	55	164	22.85	53.21

Table 2.2: A summary of relevant lengths for the cavity design chosen. ROC = radius of curvature.

Apart from the resonant frequencies condition for the two pump combs, I also accounted for cavity stability using the stability criterion of Eqs. 2.13. As discussed in Sec.1.1, there are several criteria to ensure cavity-comb coupling. In terms of this design, it was important to have the repetition rate of our laser, 100 MHz, equal the free spectral range (FSR) of the cavity. This means total cavity lengths, L, are 3 m (see Eq. 2.16).

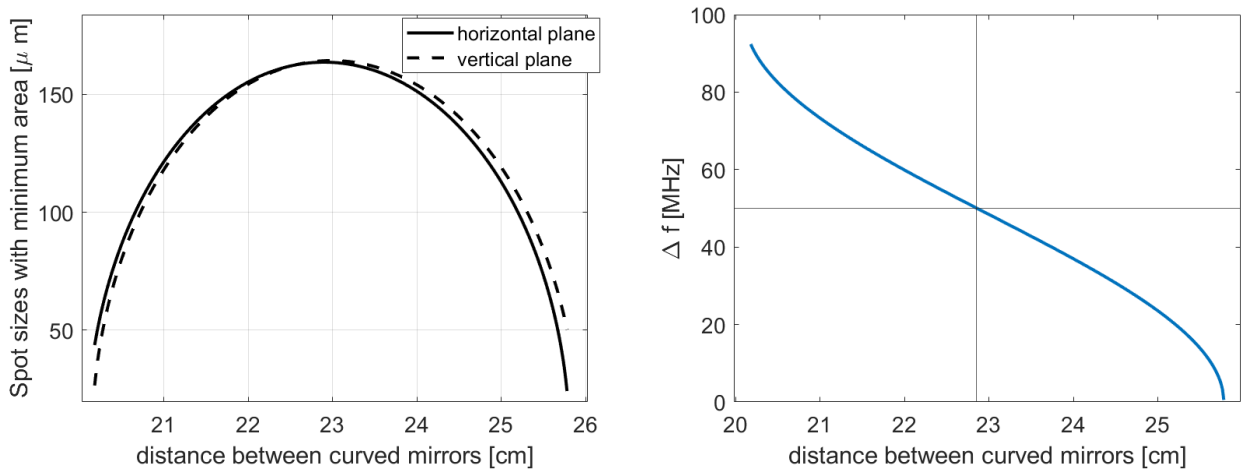

Figure 2.14: Spot sizes and Δ f between the 00 and 20 Hermite-Gaussian modes against distance between curved mirrors. In this design, we choose the largest spot sizes while also choosing for the curved mirror separation that means the Δf between the resonant modes for the 00 and 20 Hermite Gaussian modes is 50 MHz. This is shown as the point where the two vertical lines cross and corresponds to the separation stated in 2.2.

$$FSR = \frac{c}{L} \tag{2.16}$$

The cavity geometry also determines the waist size at the focus; I tried to minimize this waist in the probe cavities by choosing mirrors with the smallest possibly radius of curvature with the constraint of not clipping the nozzle cup where the molecular beam will be released. This cup is a 2 inch diameter inner vacuum chamber, which allows us to differentially pump to lower background pressure and reduce possibilities of cavity mirror contamination. The beams must also maintain angles of incidence on each mirror of less than or equal to 3°. However, in the case used in this design, the beams just miss the edges of the cup. More planning and considerations can be made to reduce the possibility of grazing the cup, or to decide desired waist sizes more carefully and whether the same cup in use is needed or a smaller cup can be used.

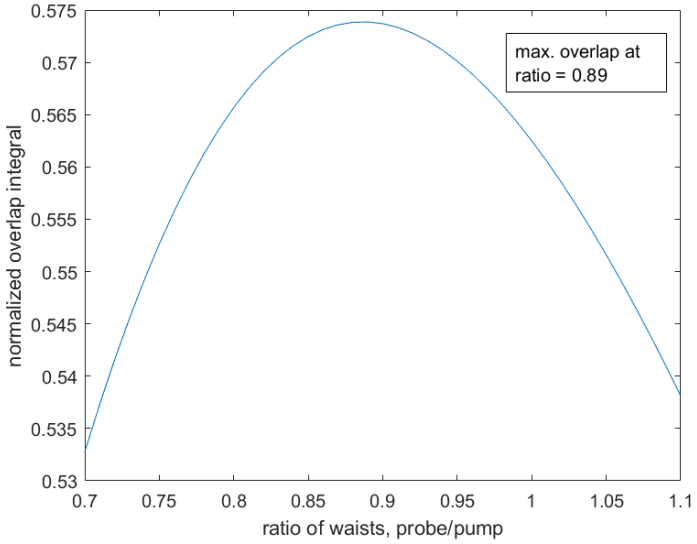

Figure 2.15: The overlap integral between the two pump modes and the probe mode as a function of ratio of their $1/e^2$ waists. This preliminary calculation indicates that maximum overlap occurs when the probe waist is about 0.89 times the size of the pump waist. However, having the waists be the same size does not dramatically decrease their overlap. This overlap is calculated by integrating across the different Hermite-Gaussian modes involved and normalizing the overlap integral. In this calculation, the pump beams are assumed to be in the TEM00 and TEM20 modes, and the probe in the TEM00 mode.

Another possible question to explore is that of the requirements for the probe cavity. In the current design, the probe cavity is identical to the pump cavity. In Fig. 2.15, I plot the result of an spatial overlap integral between the pump and probe waists. This integral is given by:

$$\text{Overlap} = \frac{\int dx \int dy (u_{00}^{\text{pump}} u_{20}^{\text{pump}} u_{00}^{\text{probe}})}{\sqrt{\int dx \int dy (u_{00}^{\text{pump}} u_{00}^{\text{pump*}} u_{20}^{\text{pump}} u_{20}^{\text{pump*}} u_{00}^{\text{probe}} u_{00}^{\text{probe*}})}} \tag{2.17}$$

Here the numerator is a spatial overlap between the three different beams. The denominator here is a normalization factor. In the calculation of Fig. 2.15, I keep the probe size constant and integrate 2.17 over a range of pump sizes. Each 'u' here is a function of the size of the beam and the Hermite-Gaussian beam, and is given by:

$$u_{nm}(x,y) = \sqrt{\frac{2}{\pi}} \sqrt{\frac{1}{2^{n+m} w_{0x} n! w_{0y} m!}} H_n\left(\frac{\sqrt{2}x}{w_{0x}}\right) H_m\left(\frac{\sqrt{2}y}{w_{0y}}\right) e^{-x^2/w_{0x}^2} e^{-y^2/w_{0y}^2} \tag{2.18}$$

Here, 'n' and 'm' are the same Hermite-Gaussian mode numbers discussed above, H_n is the

n^{th} order Hermite polynomial, H_m the m^{th} order Hermite polynomial, w_{0x} and w_{0y} are the $1/e^2$ intensity radii of the fundamental TEM00 mode in the x and y directions [17].

Fig. 2.15 suggests that higher spatial overlap would occur if the probe waist was slightly smaller than the pump waist. This was not implemented in the current design because the cavity parameters chosen pushed the edge of how small a waist seemed attainable with the current cup. In any case, this design can act as a reasonable starting point from which more optimal conditions can be chosen during the actual build.

3 Absorption and Pressure

In discussions of considerations of nozzle size and placement, a question that came up is that of how low background pressures the experiment would need to avoid pulse distortion by absorption from molecules in this background. More details on this issue are portrayed in Figs. 3.1 and 3.2. This would inform whether the molecule delivery system would require serious redesign for the proposed experiment. We know that at high pressures, absorption features are broad and can absorb most of the energy in an input pulse. In that case, 'background' molecular signals can completely distort pulses and leave one unable to resolve the actual signals of interest.

In the following discussion, I consider the absorption features of water as would be relevant for future 2DIR spectroscopy of water clusters.

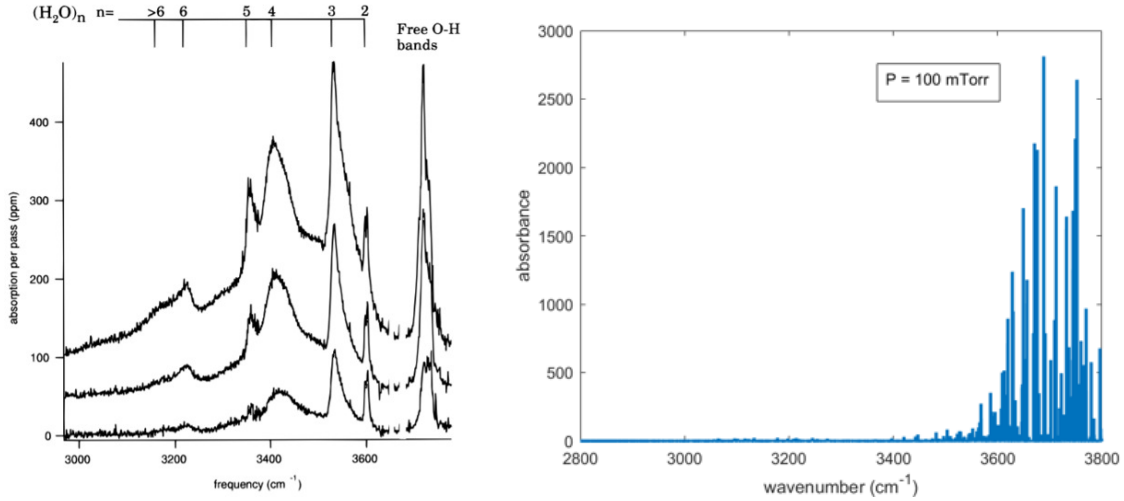

Figure 3.1: Linear absorption spectrum for various $(H_2O)_n$ clusters obtained by cavity ringdown laser absorption spectroscopy by Paul et. al. [29] on the left and absorbance for the H_2O molecule at 100 mTorr on the right. Absorbance here is the product of the absorption coefficient and interaction length (here, assumed to be 3 m); this is the argument of the exponential in Eq. 3.1. Essentially, should the absorbance represented on the right be high enough, the background water molecules may absorb all of the energy in the incoming beam and one would not be able to decipher the absorption features that result from the water clusters of interest. Calculation used to produce right figure uses data from HITRAN database [30]. Left figure taken from Ref. [29].

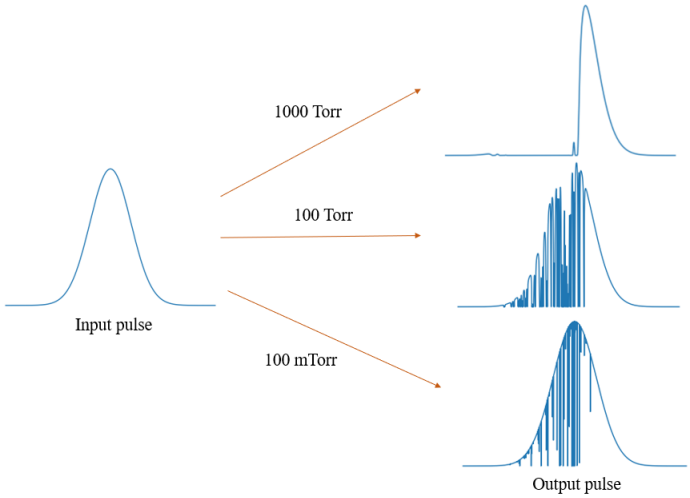

Figure 3.2: A diagrammatic representation of the issue at hand, in the frequency domain. Each output pulse corresponds to a different partial pressures (as labelled). At different partial pressures, the density of background molecules is different. At high pressures, like 1000 Torr, most of the energy of the pulse is absorbed. But at lower pressures, like 100 mTorr, the absorption lines are less wide but still strong. It is not immediately obvious how this affects pulse energy and distorts the pulse in the time domain. The subtlety of the question then becomes that of how narrow but strong lines affect pulse shapes in the time domain, and energy.

3.1 Absorption Coefficients

At first, I considered how absorption cross sections changed at different partial pressures. The absorption cross section is a value that can be understood in terms of the Beer-Lambert Law, which states that the intensity of light through an absorbing medium decays exponentially according to Eq. 3.1 [31]. In this equation, I is the intensity after absorption, I_0 the intensity before absorption, α is the absorption coefficient and l the length of the absorbing medium the light crosses through. α effectively measures how strongly a medium absorbs light.

$$I = I_0 e^{-\alpha l} \tag{3.1}$$

The thought here was that if absorption coefficient were generally low at pressures we generally operate at in the present experiment (cavity-enhanced UV-Vis spectroscopy), one would safely know absorption effects would not greatly distort pulses.

Absorption coefficients were calculated using data retrieved from the HITRAN database [30]. More specifically, line strength values retrieved from the database were used along with a Voigt

lineshape to determine the absorption coefficient as is explained on the HITRAN website [32]. The lineshape is a function of pressure.

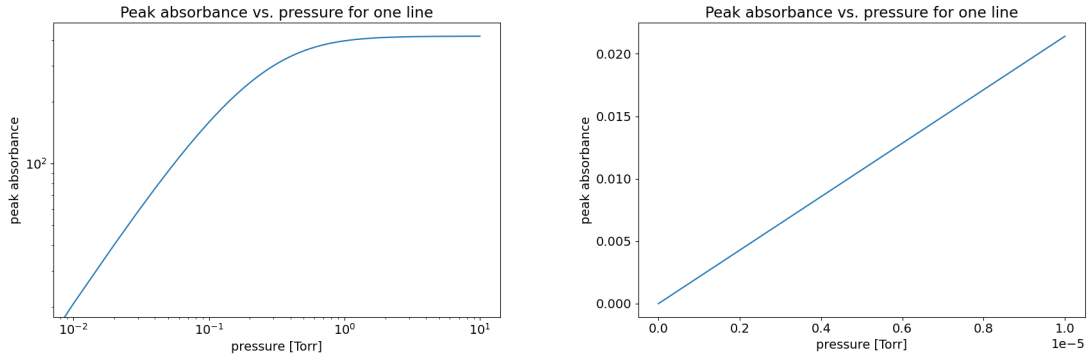

Figure 3.3: Peak absorbances vs. pressure. These figures show the value for the peak absorbance of a line centered at 3752 cm^{-1}. I choose this line because it has the highest line strength in the 3 to 5 µm range. The path length, l, is taken as 3 m here. The figure on the left shows results for pressures from 0.01 Torr to 10 Torr, while the figure on the right only from the 0 to 10 μTorr range. The point being here that to achieve peak absorbances of 0.01, or 1%, this calculation suggests one needs to be at around 5 μTorr.

As indicated in Fig. 3.3, simple calculations based on the absorption coefficient alone indicated that the experiment would have to achieve extremely low pressures on the order of μTorrs. However, the method of looking at absorption coefficients alone does not actually capture what happens to the pulse on absorption.

3.2 Complex Refractive Index

A more sophisticated model considers absorption through the effect of the complex refractive index. That is, after absorption, a pulse, $E(\omega)$ becomes

$$E(\omega)e^{i\tilde{n}(\omega)\frac{\omega}{c}z} \tag{3.2}$$

Here, ω is the frequency of light, c the speed of light, z the distance propagated in the absorbing medium, ñ the complex refractive index. The specific information about the absorbing line is contained in ñ, which is defined in the following way [33]:

$$\tilde{n} = n' + i\kappa \tag{3.3}$$

Here n', the real part of the complex refractive index ñ contains information about dispersion of the pulse and κ, the imaginary part of the ñ, information about absorption. This can be seen by inserting Eq. 3.3 into Eq. 3.2.

$$E'(\omega) = E(\omega)e^{i\tilde{n}(\omega)\frac{\omega}{c}z} = E(\omega)e^{in'(\omega)\frac{\omega}{c}z}e^{-\kappa\frac{\omega}{c}z} \tag{3.4}$$

That is, $E(\omega)$ is attenuated by κ, the imaginary part of ñ, and n' adds phase to the pulse/wave, i.e. controls its dispersion. κ is directly related to the absorption coefficient discussed earlier in this text in the following way:

$$\alpha = 2\kappa k_0 \tag{3.5}$$

Here, k_0 is the center wavenumber of the relevant absorption line.

n' and κ are related to a complex lineshape, $f(\omega)$, in the following way.

$$n' \propto Im[f(\omega)] \tag{3.6}$$

$$\kappa \propto Re[f(\omega)] \tag{3.7}$$

Using HITRAN definitions [32], the relevant proportionality constant is $SN/(2k_0)$, where S is the "spectral line intensity", N the number density of the molecules at a given pressure and k_0 the center wavenumber for the absorption line.

In my modelling, I use a complex Voigt profile as my lineshape $f(\omega)$ [34]. The Voigt profile is the convolution of a Lorentzian and Gaussian profile; at low pressures, it is dominated by the Gaussian profile and at high pressures, by the Lorentzian profile which is in keeping of understandings of pressure effects on lineshapes [31]. The complex Voigt profile can also be described as the following:

$$V(\omega;\sigma,\gamma) = \frac{w(\omega-\omega_0)}{\sigma\sqrt{2\pi}} \tag{3.8}$$

Here, σ is the Gaussian Doppler width of the profile, γ the Lorentzian pressured-broadened width and w$(\omega-\omega_0)$ the Faddeeva function evaluated at $\frac{(\omega-\omega_0)+i\gamma}{\sigma\sqrt{2}}$. This is a more tractable

definition of the complex Voigt profile as the Faddeeva function is easily evaluated using functions in a computation library like SciPy in Python.

Having defined the complex refractive index as needed, to simulate the effect of absorption in the time domain, one would, in theory, only have to take an inverse Fourier transform of Eq. 3.3. The effect of each absorption line in the pulse's bandwidth would be captured by a sum of complex refractive indices in the exponent. An example illustrating this idea is shown in Fig. 3.4. However, given the linewidths of these absorption features, sampling the pulse in the frequency domain would mean sampling a bandwidth of around 10^8 MHz (for a 100 fs pulse in the time domain) with 1 MHz precision. This would require 10^8 i.e. 100 million points, which is not tractable with the computation tools available. So, the direct Fourier transform method to determine pulse distortion in the time domain is not feasible.

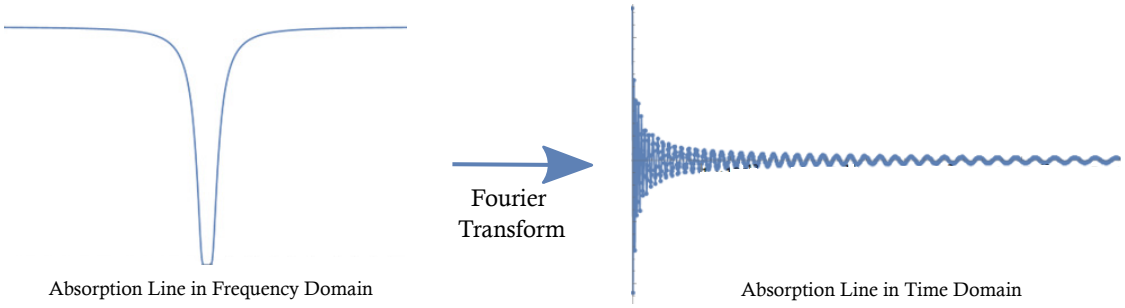

Figure 3.4: For example, the effect of one absorption line in Eq. 3.3 in the frequency domain would lead to a notch in the pulse represented here on the left (only the exponential function, i.e. the Green's function is considered here). The figure on the right is only a representation of the first figure's inverse Fourier transform, and is identical to the free induction decays observed in MRI imaging. The frequency of the carrier in the time domain is center frequency of the line in the frequency domain. The computation problem in directly taking a Fourier transform for multiple lines is explained in the text above.

3.3 An Analytic Approach

Instead of having the numerically find the inverse Fourier transform of Eq. 3.3, we instead turn to an analytic form of the inverse Fourier transform.

In work done on modelling Mössbauer transitions in the time domain by van Burck et. al. in 1992 [35], the authors also employ a complex refractive index, and its inverse Fourier transform, to describe the X-ray resonances in ^{57}Fe. They obtain an analytic form of the inverse Fourier transform from an earlier work by Kagan et. al. in 1997 [36]. Kagan and colleagues also model

X-ray resonances as are relevant for Mössbauer spectroscopy.

An important approximation they make in simplifying the problem is approximating the spectrum as a constant over each line in the frequency domain. That is, because the absorption line is so narrow compared to the pulse bandwidth (which posed problems in directly taking numerical transformations as discussed in the previous sections), we can approximate the pulse amplitude as constant over the the width of the line. That is, for each line, we assume the following:

$$E(\omega)e^{i\tilde{n}\frac{\omega}{c}z} = E(\omega_0)e^{i\tilde{n}\frac{\omega}{c}z} \tag{3.9}$$

Here, $E(\omega_0)$ is the electric field of the pulse at the center frequency for the given line, which is a constant value.

In Kagan et. al.'s work, they find an analytic form for the relevant inverse Fourier transform using complex analysis techniques. They also subtract this response function from the original pulse in the time domain. This is because their approach is to essentially find the inverse Fourier transform of the absorption lines themselves, and subtract those responses from the original pulse, which is an idea similar to that of Babinet's principle.

Adapting Kagan et. al.'s approach to the problem at hand and using their result as a Green's function, we write our response function (i.e. the pulse in the time domain) as

$$R(t) = A(t)e^{-i\omega_c t}e^{i\phi(\omega_c)} - \sum_n e^{-i(\omega_n t - \phi(\omega_n))}f(t)E(\omega_n) \tag{3.10}$$

A(t) is the pulse envelope (in time), ω_c the carrier frequency of the pulse, $\phi(\omega_c)$ the phase associated with that carrier frequency i.e. $(\omega_c/c)z$, ω_n the center frequency for each absorption line considered with its corresponding phase $\phi(\omega_n) = n'(\omega_n)(\omega_n/c)z$, $E(\omega_n)$ the amplitude of the pulse envelope at ω_n and f(t) is given by a result derived by Kagan et. al.:

$$f(t) = e^{-\tau/2}\frac{\xi}{\tau_0}\frac{J_1(2\sqrt{\xi\tau})}{\sqrt{\xi\tau}}\theta(t) \tag{3.11}$$

Here τ_0 is $1/\gamma$, where γ is the linewidth of the absorption line, $\tau = t/\tau_0$, $\xi = \frac{l}{4}\alpha$ (l is the total path length the pulse travels through, which is 3 m in step of the calculation, α is the peak absorption coefficient, ξ is also defined this way in Ref. [35]), J_1 is a Bessel function of the first

kind and $\theta(t)$ a step function.

As Eq. 3.10 implies, in this analysis, one finds the total response function by finding Eq. 3.11 for each line, taking a sum of each line's contribution and subtracting it from the original pulse with dispersion. α in the value of ξ and the dispersion are functions of pressure and number density.

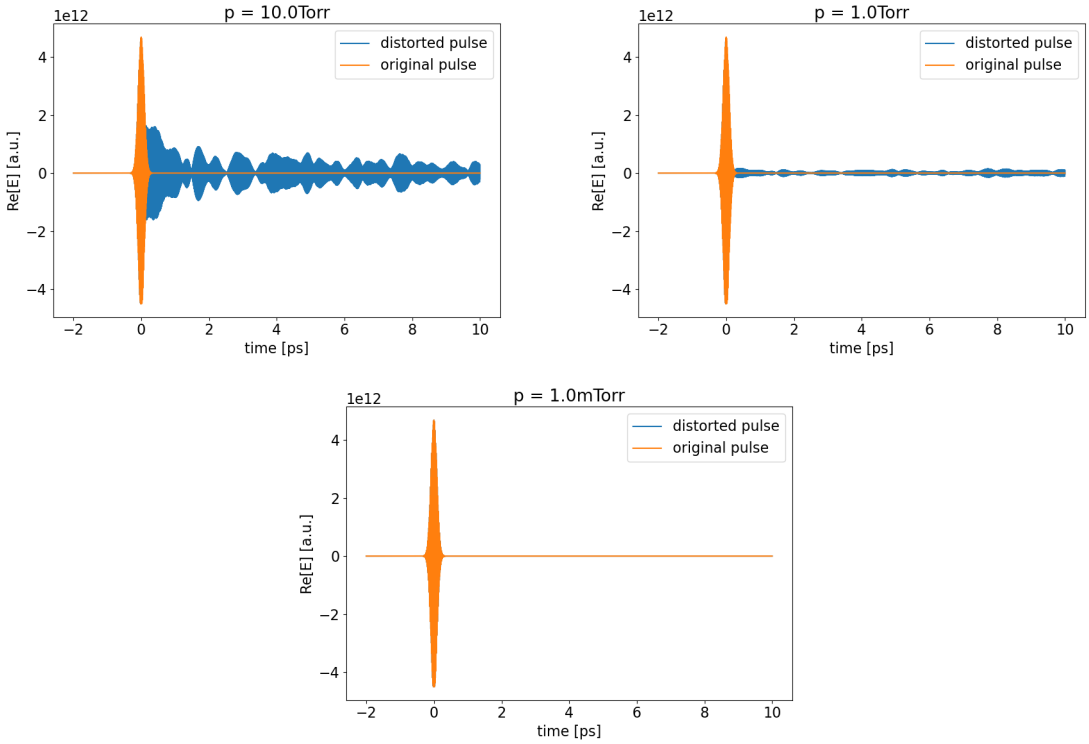

Figure 3.5: Results of calculating Eq. 3.10 with a Gaussian pulse of 100 fs duration, with a carrier frequency of 1.12×10^8 MHz and applying absorption features within its bandwidth. At a very high partial pressure of ambient water of 10 Torr, the pulse is highly distorted and loses a lot of energy; this effect becomes less strong at decreasing pressures.

3.3.1 Estimating Loss

The results of these calculations can also provide an estimate of how much energy is lost with different partial pressures of water. This also provides a more quantitative measure of how severe pulse distortion is in each case. Energy loss is estimated using the following equation:

$$\text{loss} = 1 - \frac{\int I_{\text{distorted}} dt}{\int I_{\text{original}} dt} \tag{3.12}$$

where $I_{\text{distorted}}$ is the intensity of the distorted pulse, and I_{original} the intensity of the original

pulse.

Losses calculated using this method were also verified by using a more straightforward method of estimating loss where I subtracted the total energy contained in each absorption line, by integrating the intensity in the frequency domain, and subtracted the sum from the total energy contained in the pulse.

To make calculations more closely match the actual experiment, two further modifications were made to the model.

The first was to account for the finesse of the cavity in a simple way. That is, the path length the pulse travels through was defined at the total cavity length in the first phase of calculations. However, the fact that our pulses will circulate in an enhancement cavity mean that the actual path length they travel will be greater than just the length of the cavity. We estimate that the cavity enhances the path length pulses travel by a factor of $\mathcal{F}/\pi$, so the following estimates were made by scaling path lengths by $\mathcal{F}/\pi$.

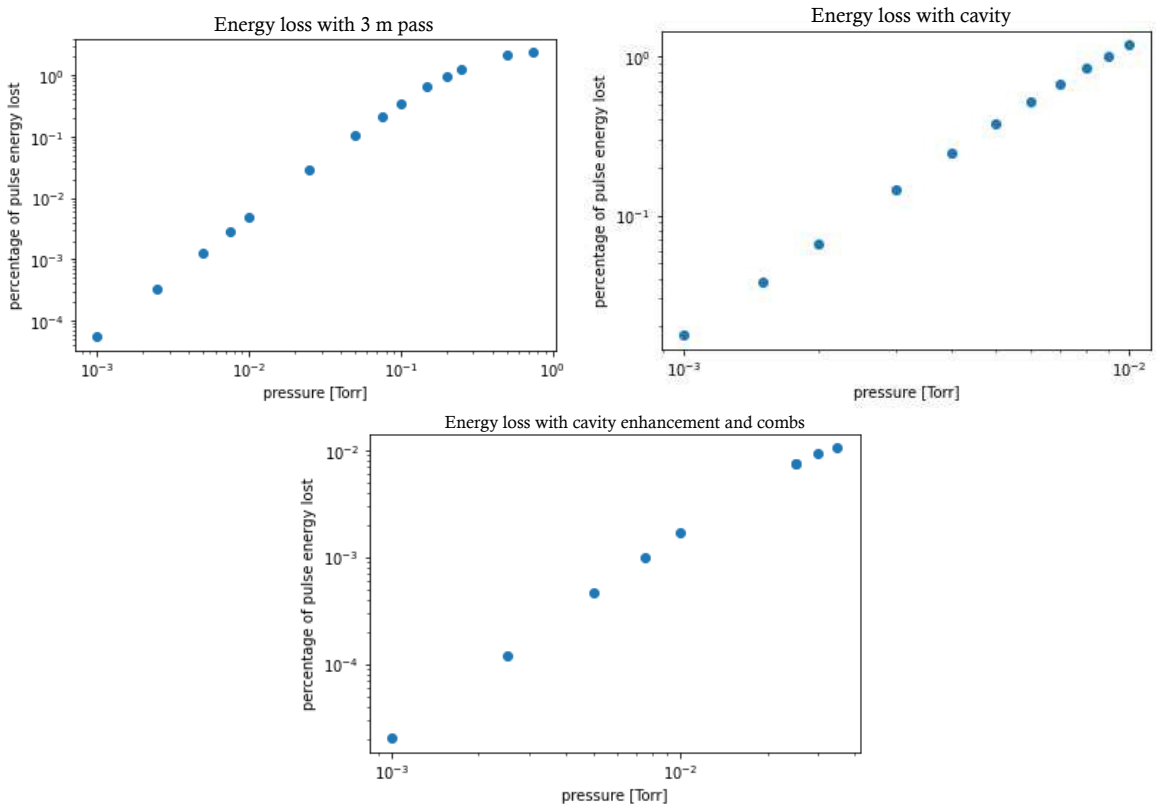

Figure 3.6: Energy loss computed for a range of different pressures in the three different sets of conditions considered. The top left plot is a result of calculations without any cavity/comb considerations but just assuming the light has a 3 m interaction length with the molecules causing the background absorption. In this case, 1% energy loss occurs at a partial pressure of around 200 mTorr. The top right plot adds the cavity enhancement factor to this interaction length. 1% energy loss occurs at a partial pressure of around 9 mTorr. Finally, the bottom plot accounts for both cavity enhancement and frequency combs. 1% energy loss occurs at a partial pressure of around 35 mTorr.

The second modification made was to account for the fact that our pulses are from a frequency comb. That is, in the frequency domain, we do not span a continuum of frequencies but discrete frequencies that are regularly separated. So, calculations made without accounting for the comb would overestimate pulse distortion and energy loss as they assume a continuum of frequencies. The comb nature of our laser is an advantage in this case because each absorption line only interacts with a few comb teeth, depending on the width of the absorption line. If the absorption line is much narrower than the spacing between comb teeth and far from a comb frequency, the line becomes irrelevant to the problem. For example, at 1 Torr, the maximum linewidth is 139 MHz, which means it would only span approximately two comb teeth at most (the separation between

the teeth is 100 MHz). At lower pressures, say at 100 mTorr where the maximum linewidth was 13.9 MHz, this effect is even stronger.

In terms of the accounting for the comb in this calculation, I do so by changing the function that represents $E(\omega_n)$ that multiplies $f(t)$ in Eq. 3.10. The function models the pulse in the frequency domain as regularly separated Gaussians with 10 kHz bandwidths, and returns the sum of the value of these Gaussians at the specified ω_n, the center for the given absorption feature.

3.3.2 Autocorrelations

In ultrafast spectroscopy experiments, the molecular response is convolved with the instrument response [37], which for a pump/probe measurement is the convolution of the pulse with itself. So, another relevant metric in this discussion is the autocorrelation of the pulse after absorption; this tells us how much the pulse distortion matters to the measurement.

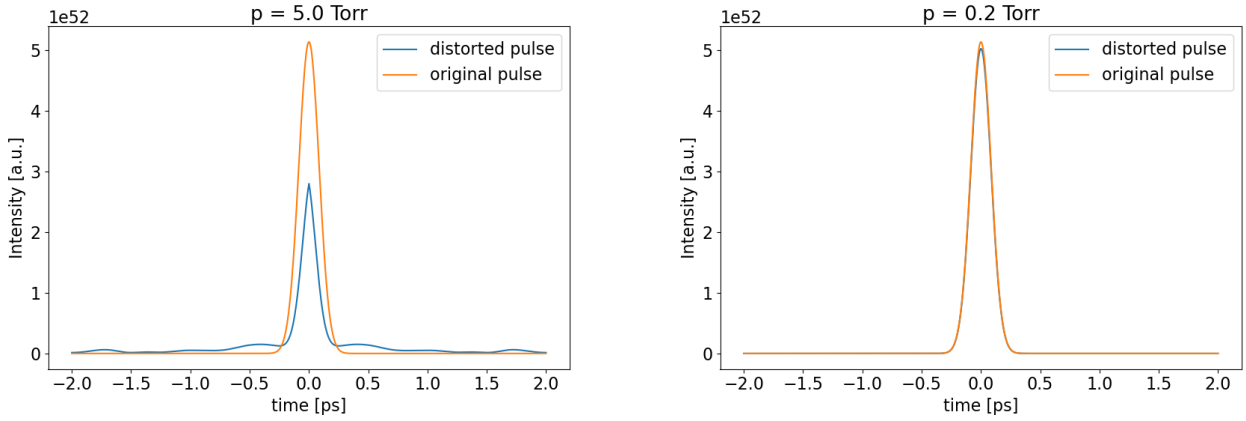

Figure 3.7: A comparison of the intensity autocorrelations in cases where absorption distorts the pulse greatly and when very little of pulse is absorbed. This was calculated without any consideration of the cavity and frequency comb nature of the pulses. In the case of high absorption, the height of the pulse is much shorter than the original pulse and energy is carried away in its tails.

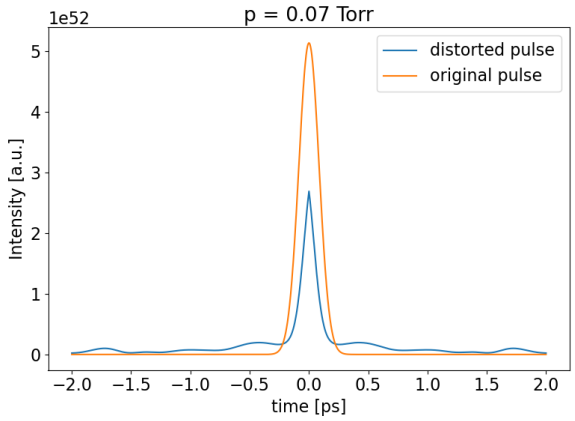

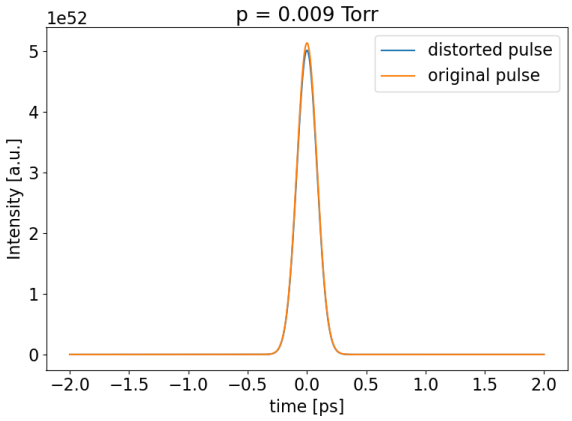

Figure 3.8: A similar comparison to that in Fig. 3.7 but now with a factor of finesse in the path length for the pulses. A similar trend is observed here as in Fig. 3.7, however, energy loss is high at a much lower pressure of 70 mTorr (vs. 5 Torr in Fig. 3.7).

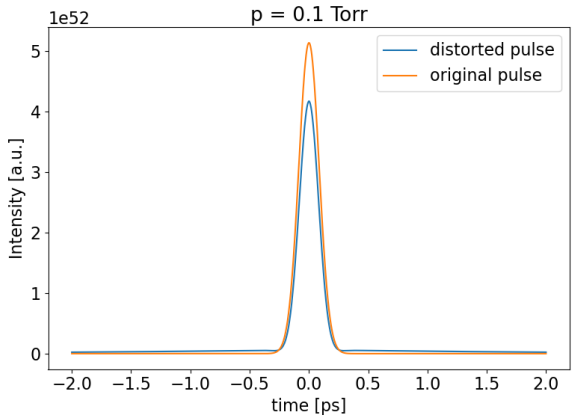

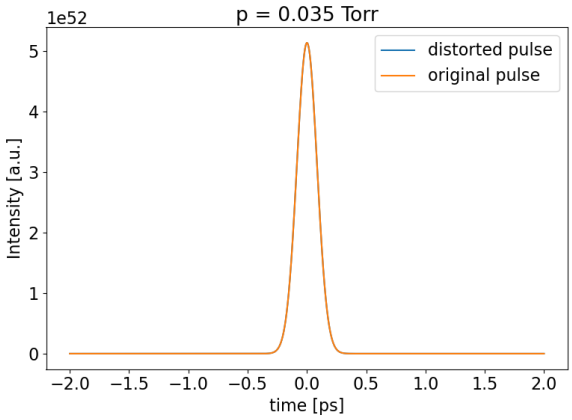

Figure 3.9: Autocorrelations in the case of accounting for both the cavity finesse and the comb properties of the pulses. Here, at higher pressures such as 100 mTorr, the autocorrelation indicates that the pulse loses energy as expected but does not have the same wings shown in the other two cases above.

4 Fiber Laser Development

In this final chapter, I detail my contributions to the fiber laser development needed to create mid-IR light for the cavity-enhanced 2DIR experiment. We will derive two signal branches in the 1.3 to 1.7 µm range from our 1.5 µm frequency comb. These two branches along with an existing 1.06 µm will drive the OPAs discussed in Sec. 1.4 and Sec. 2.1. Details of the components in these branches are shown in Fig. 4.1. A background for the propagation of light in fibers as is relevant here is provided in Sec. 1.3. My work, in particular, focuses on integrating components needed to create light in the mid-IR and shifting the f_0 of one of our signal combs.

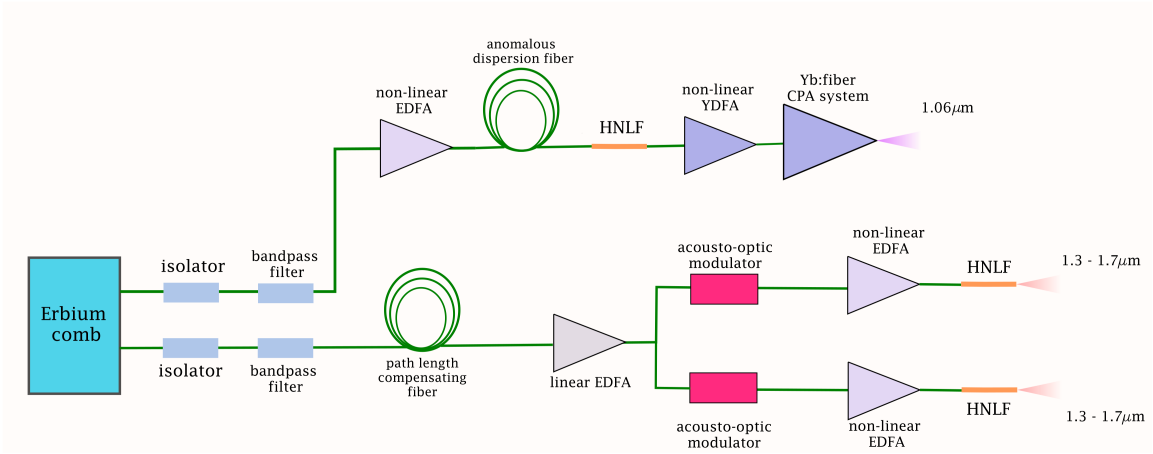

Figure 4.1: For the 2DIR experiment, we will derive two signal and one pump comb from our 100 MHz Erbium comb. The pump (1060 nm) branch was built for other experiments so is already in existence. The two signal branches come from the same main branch from the oscillator and are split as two different outputs out of linear EDFA. Before the linear EDFA, we will use path-length compensating fiber to have the same pump and signal pulses from the oscillator reach the OPA. We also use a linear erbium-doped fiber amplifier (EDFA) to amplify the power entering the AOMs to compensate for power loss through them. The two output branches are then amplified and broadened in non-linear EDFAs. After these amplifiers, the beams are launched into highly non-linear fiber (HNLF) to generate light across the bandwidth desired for the signal branch.
Each signal beam will be used along with the pump beam for DFG in the OPAs as shown in Fig. 2.1. In reference to Fig. 1.4, the pump here is 'ω_1', the signal 'ω_2' and the generated idler the difference of the two.

4.1 Path-Length Compensation

As Fig. 4.1 illustrates, while the pump and signal beams originate from the same frequency comb, they travel through different components and paths before they meet again at the PPLN crystal. What this means is that the pulses that overlap at the PPLN may not have left the oscillator at

the same time. Any fluctuations in the repetition rate will affect the time delay between the pulses that overlap at the crystal. We also match the repetition rate of our cavity to that of the oscillator through feedback control and this process may add different noise to different pulses. Further, different pulses will inherently have different phase fluctuations. We would like to minimize all sources of noise.

To avoid these possible issues, we can have the optical path lengths for the signal and pump match exactly and have the pulses that meet at the crystal be pulses that leave the oscillator at the same time. We do this by determining the optical path length difference between the two branches and adding fiber to the shorter (in this case, signal) branch to compensate for its path length.

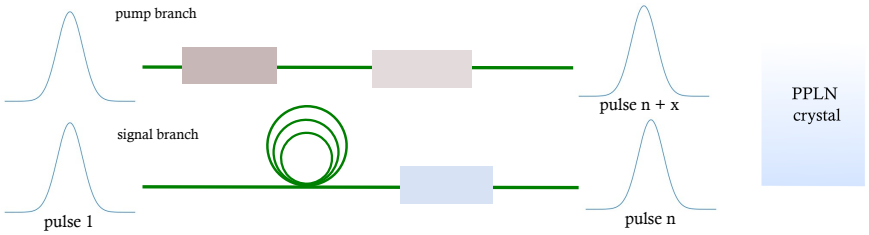

Figure 4.2: An illustration of the path length difference issue. As the pump and signal branches include different components and paths, the pulses that meet at the crystal may not originate from the same pulse in time. For example, if pulse n is incident on the crystal from the signal branch, the pump pulse may be some pulse x cycles later. The purpose of this measurement is to determine this 'x'.

The time delay between pulses that travel different path-length is

$$\Delta t = \frac{\Delta n}{f_{rep}} + \Delta T \tag{4.1}$$

The first term in Eq. 4.1 results from the offset in pulses, Δn. The second term, ΔT, accounts for any additional path-length difference that may result from different in-fiber or free-space propagation.

If we take the derivative of Eq. 4.1 with respect to f_{rep}, we get

$$\frac{\Delta(\Delta t)}{\Delta f_{rep}} = -\frac{\Delta n}{f_{rep}^2}$$

$$\Delta(\Delta t) = -\frac{\Delta n}{f_{rep}^2}\Delta f_{rep} \tag{4.2}$$

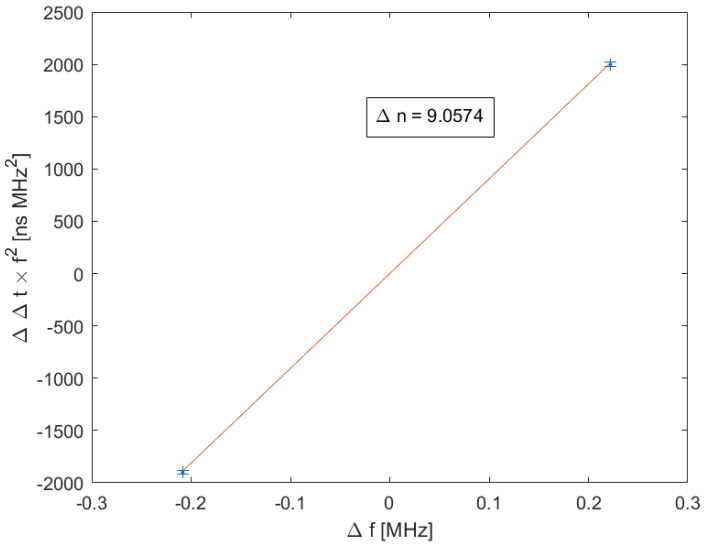

Figure 4.3: A straight line defined by two measurement points and Eq. 4.2 suggests a Δn of approximately 9. For fiber with refractive index of approximately 1.5, this suggests needing 18 m of path-length compensation. Error bars shown come from the precision of the sampling scope and frequency counter used to make these measurements.

That is, if we change the repetition rate of the oscillator, the change in the time difference between the arrival of the different pulses at a point scales with Δn. So, to determine Δn, I changed the repetition rate and measured how the time delay between the pump and signal branch changed.

The results of this measurement are shown in Fig. 4.3. For a change in about 200 kHz in repetition rate, the time separation between the pump and signal changes by about 200 ps. These measurements were also verified by additional path-length to the signal branch, and noting now Δn changed for the amount of fiber added. Following the results obtained (of n = 9), the following testing and development, 15 m of PM-980 path compensating fiber between the bandpass filter and linear EDFA was used, this is as shown in Fig. 4.1.

4.2 Linear Pre-Amp and AOM

The linear EDFA that precedes the AOMs was mostly assembled – I characterized its behavior and made modifications to complete its assembly.

Important modifications made to the pre-amp include choosing to pump the amplifier backwards and splicing the pump fiber directly to the wavelength division multiplexer (WDM) (instead of

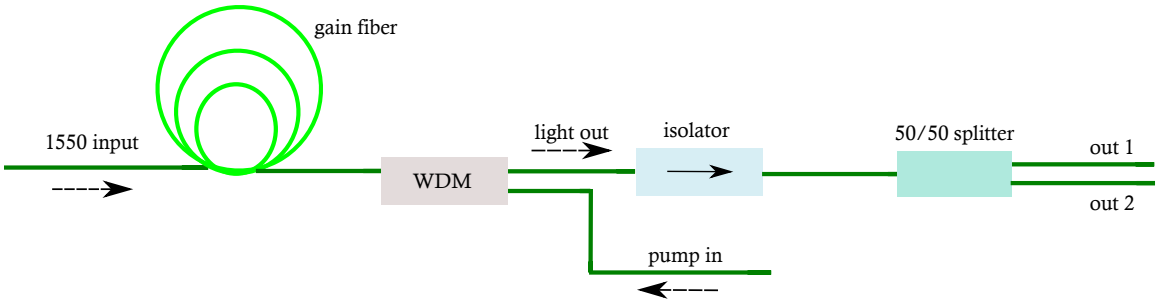

Figure 4.4: A diagram of the final configuration used for the pre-amp. The direction of light is shown with dashed arrows. Here, WDM is a wavelength division multiplexer used to have the input travel in the same fiber as the pump for the amplifier. The length of the gain fiber is about 99 cm. The total length of fiber running from the input to each output is about 3.35 m.

having a connector on the amplifier's box) for better performance. We chose to pump the linear EDFA backwards because we compared the performance of another EDFA in use in the group with a similar design as the linear EDFA in question when it was pumped forwards and backwards. From those measurements, we determined that the EDFA performed better when pumped backwards rather than forwards. I also added a 50/50 splitter to the output of the amplifier to have two outputs.

pump current [mA]	output 1 [mW]	output 2 [mW]
200	0.51	0.44
400	5.34	4.49
500	8.45	7.16
1000	25.78	21.50
1200	33.05	27.17

Table 4.1: Characterizing the power out of the pre-amplifier's two outputs; this information allows one to choose an appropriate pump power to compensate for power loss in the AOM.

The next step in assembling this part of the signal branch was to test using the pre-amplifier with the AOM, and setting up the RF amplifiers and electronics required for running the AOM.

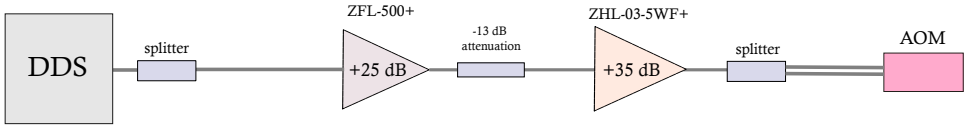

Figure 4.5: The assembly of RF electronics used to drive the AOM. This setup supplies approximately 1 W (30 dBm) of power to each RF input of the AOM. Part numbers for the RF amplifiers from Mini-Circuits Technologies Sdn. Bhd. are shown above the amplifiers.

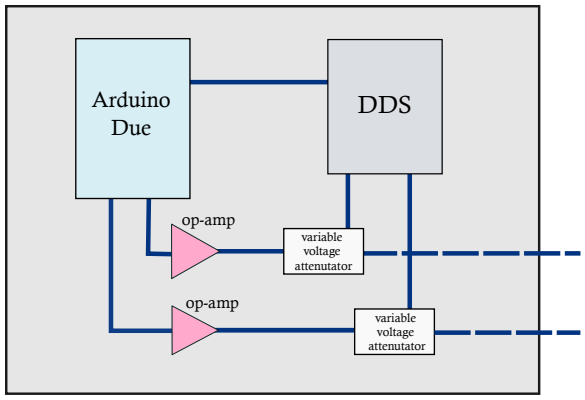

Figure 4.6: A simplified schematic of the setup used to control the direct digital synthesizer (DDS) and adjust the RF power from it. The DDS (part number: AD9958) produces an RF sine wave from a digital input from the Arduino. The DDS is clocked by the 100 MHz Menlo oscillator (connection not shown here). The Arduino controls both the DDS inputs and the variable voltage attenuators (part number: HMC346AMS8GE). The attenuators attentuate the output from the RF power to the AOM such that the AOM optical power is kept flat across a range of driving RF frequencies (see Table 4.2). The RF frequency itself is controlled by the Arduino and a potentiometer connected to it. The two outputs from this setup are shown with the dashed lines.

In addition, as we tune the signal/idler branch, the f_0 of the cavity for the changing wavelengths changes and the AOM must be able to follow these changes. At the same time, we do not want the optical power in the signal branch to shift dramatically so the AOM's output should stay relatively flat across the RF tuning range. The electronics shown in Fig. 4.6 address this issue; here, we control the output from the DDS such that the driving RF power results in roughly the same output optical power across the tuning range. A test of this control mechanism is shown in Table 4.2.

DDS freq. [MHz]	AOM power output [mW]	loss [dB]
79.1	1.494	-11.7
88.6	1.494	-11.7
94.8	1.536	-11.6
104.4	1.625	-11.3
115.0	1.478	-11.7

Table 4.2: Testing the AOM's insertion loss across the DDS frequency output range (roughly 75 to 115 MHz). The AOM's loss remains roughly uniform. Loss here assumes the optical power in (from the pre-amp being pumped with 1000 mA) is about 22 mW.

4.3 Non-Linear EDFA Tests

Having tested and assembled the signal branch up to the AOM, the next step was to integrate the non-linear EDFA. We use this EDFA to produce a broadened spectrum with a short pulse duration and allow for the beginning of a soliton to form. A short pulse duration and high power output indicate a high peak power, which is best for the non-linear processes that occur in the highly non-linear fiber (HNLF) to form the dispersive wave we use for the signal branch.

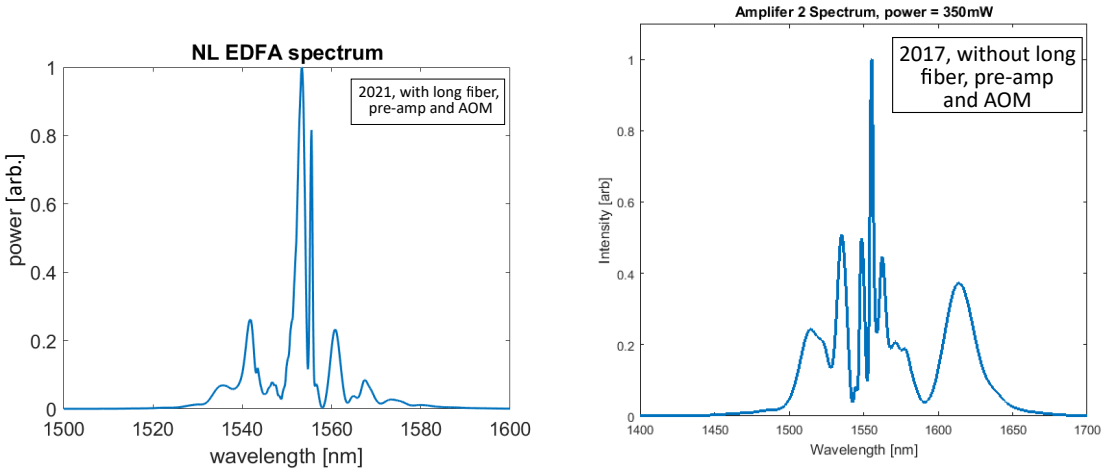

Figure 4.7: A comparison of the spectrum recorded out of a NL EDFA in 2021 during my build on the right and in 2017 during the amplifier's initial characterization on the left. First, I did not obtain as much broadening out of the amplifier. There is also not as clear evidence of the beginning of a soliton being formed; in the older spectrum this is seen in the bump formed on the red side of the spectrum. Finally, both spectra were recorded with all four pumps on the EDFA using their highest currents but the power obtained out of the amplifier in 2021 was only 290 mW at most while the power recorded in 2017 was 330 mW.

To investigate the issue of lower power out of the NL EDFA, we checked all components used including pump diodes themselves. It should be noted that the backward-pumped diodes consistently produced less power than the forward-pumped diodes and more investigation may be need to done to understand why. It then seemed like issues in the spectrum may have to do with other unintended non-linear effects or issues.

To gain some insight into what the issue may be and the nature of the pulse in time, we took an intensity autocorrelation of the spectrum shown in Fig. 4.7. The autocorrelation shown in the figure and those shown in Sec. 4.3.1 were taken with an intensity autocorrelator; the beam is first

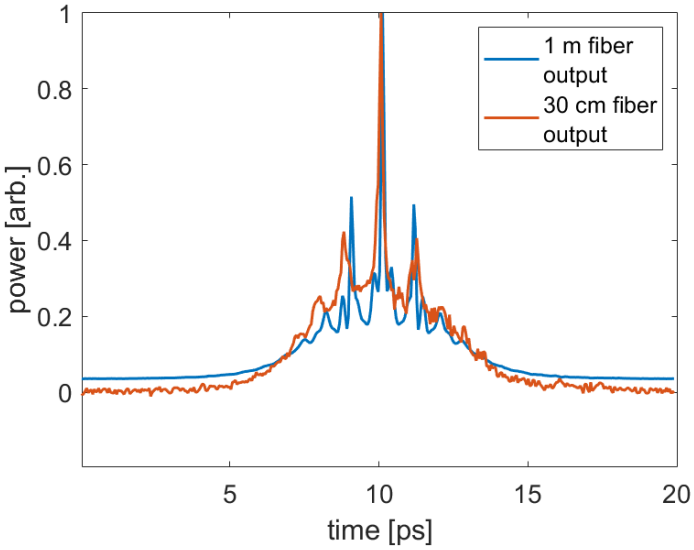

Figure 4.8: Autocorrelations obtained with two different output lengths on the NL EDFA. From this measurement, it seemed clear that unintended non-linear effects were interfering with the pulse. The side fringes seen are close to but not quite evenly spaced about the main peak.

split into two and recombined in a beta barium borate (BBO) crystal. The second harmonic (or sum frequency) that emerges hits a photodiode whose signal we retrieve. A stage is used to change the delay between the two arms that form the second harmonic and so control the generation of the light. That is, by varying the delay between the two pulses we effectively take an image of the autocorrelation of them in looking at the emergent second harmonic light.

4.3.1 Investigating the Spectrum

While we are not sure what causes the autocorrelation recorded in Fig. 4.8, we investigated many possible avenues. In this section, I document some of the various measurements as they may pertain to different phenomena. I hope they act as a starting guide for further investigation in determining a way to use the non-linear EDFA with the 100 MHz laser.

Issues considered include whether we were forming a soliton somewhere along the setup (see Fig. 4.9) and whether the long path-length compensating fiber was introducing unwanted non-linearities (see Fig. 4.10). However, as Figs. 4.9 and 4.10 illustrate, we are reasonably confident that neither of those possibilities were occurring in the setup.

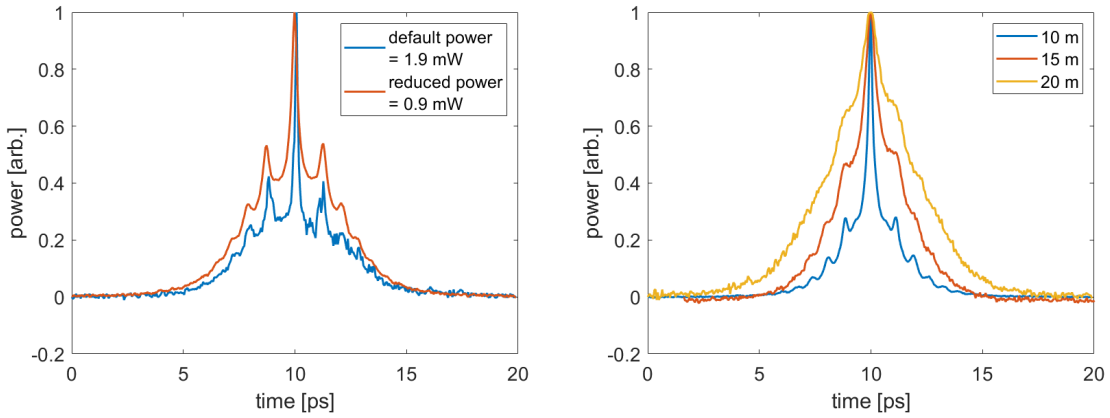

Figure 4.9: Two tests of whether we were forming a soliton somewhere along our assembly. The first plot is a comparison of the autocorrelation using two different powers from the 100 MHz laser. If we were forming a soliton, we expect its formation to depend highly on the power of the pulse. However, this comparison suggests little change in the pulse with different seed powers. The plot on the right shows autocorrelations out of the NL EDFA with different lengths for the long path-length compensating fiber. These measurements were also taken without the AOM and pre-amplifier. The pulse broadening seen for different fiber lengths roughly matches the broadening one would expect from GDD alone (calculated using linear dispersion for the PM980 fiber at 1550 nm [38]). However, if a soliton was formed, we expect the autocorrelation of the light to change dramatically with different fiber lengths as the soliton would travel away from the part of the pulse left behind, giving power-dependent satellites in the autocorrelation, which we do not observe.

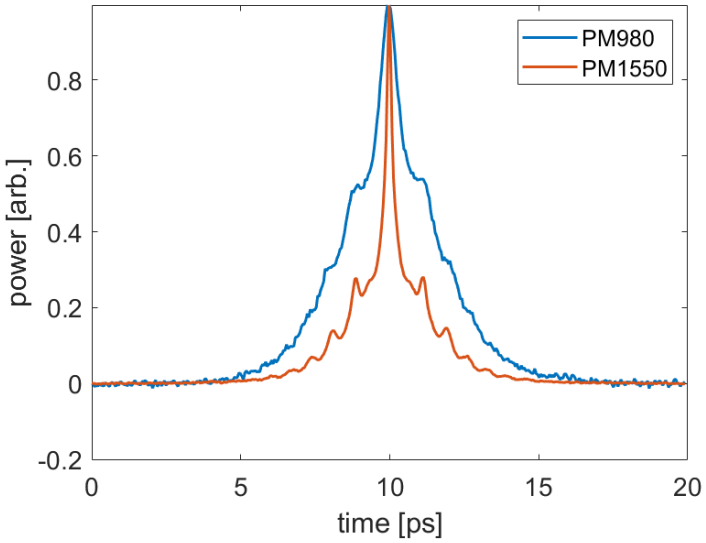

Figure 4.10: Another possible introducer of non-linearities is the long path-length compensating fiber. In this plot, we compare the autocorrelations obtained with 10 m of PM980 fiber vs. 10 m of PM1550 fiber. These measurements were also taken without the AOM and pre-amplifier. We expect the non-linearities to be different for each fiber as they guide different spectral ranges and have different mode field diameters. As we still observe the same side fringes on the autocorrelation, this comparison suggests that the long fiber is not the culprit here. Further, we would expect the second plot in Fig. 4.9 to show increased non-linearities or pulse deformation with the addition of more PM980 fiber if it was, in fact, causing the issues at hand.

Another possible question arose around the behavior of the bandpass filters used. This was partly motivated by the fact that we no longer see fringes without the bandpass filter in use (see Fig. 4.11). Further, we see notches on the spectra that emerge from the bandpass filter in Fig. 4.13 and eventually, we only obtained broadening out of the NL EDFA at powers at which this notch was diminished. In addition, the pattern of fringes on the autocorrelations remained even when using different filters (see Fig. 4.12). Further investigation can be undertaken on the performance of the filters, and how much these notches actually matter.

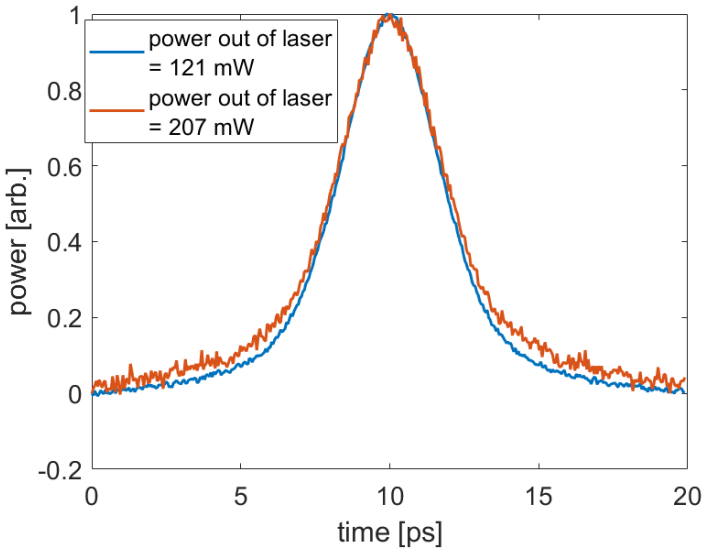

Figure 4.11: One set of measurements in which we did not observe pulse distortion/fringes. These were taken without a bandpass filter, no AOM and preamp and with 10 m of PM980 fiber. As labelled, they were also taken with different powers out of the 100 MHz oscillator/laser. This may suggest the bandpass filter disrupts the pulse in some way. However, it is possible that the pulse here is too broad spectrally for the distortions to matter.

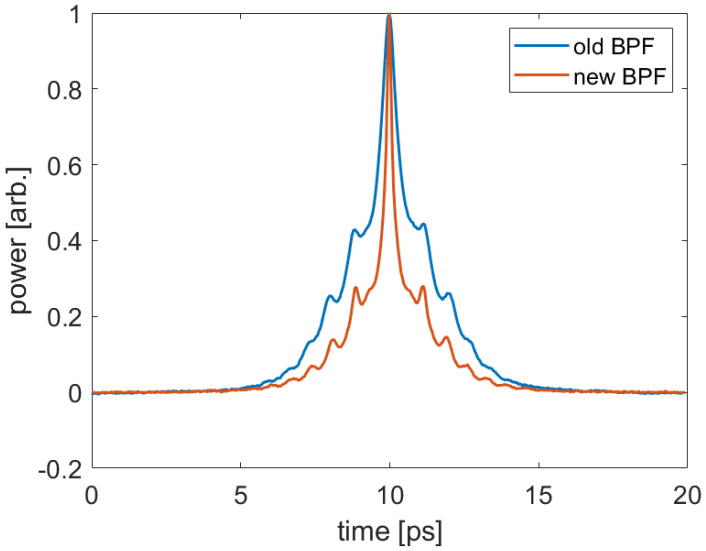

Figure 4.12: Along the lines of whether the particular bandpass filter (BPF) used distorts the pulse, I compare autocorrelations using two different bandpass filters. Both measurements were taken with the same setups, with no AOM and preamp, and 10 m of PM 980 fiber. The pulse appears to still have its now characteristic fringes on it. These filters were also purchased at two different times, so are not from the same batch.

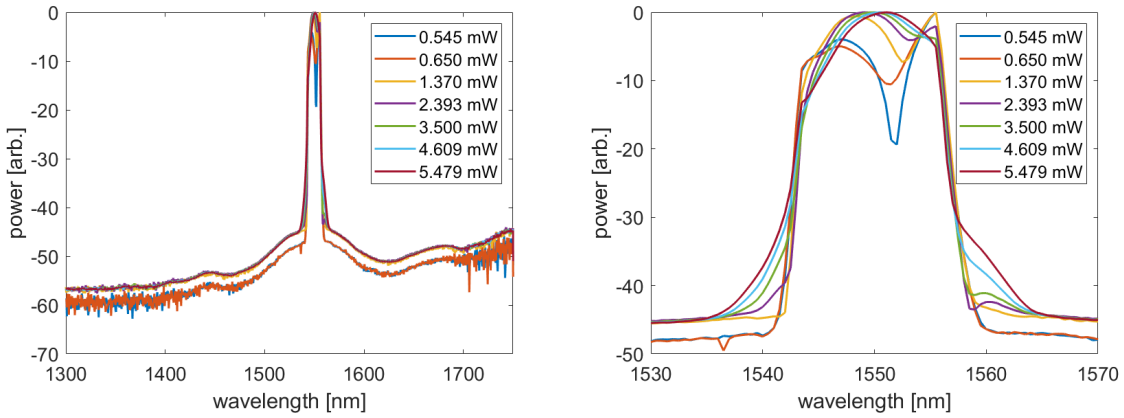

Figure 4.13: Further investigations into the possible issue of the bandpass filter. These plots show spectra recorded with the 60 MHz oscillator with the bandpass filter after it for a range of powers out of the oscillator. The first figure shows the full spectra taken and the second a zoomed-in version. Most significantly, there is a notch in the spectrum at low powers. While we do not yet know the cause of this notch, we believe it is caused by the filter itself as it is not present on the full spectrum from the oscillator at the same powers. In further tests, we find that we were able to obtain better spectra (pulse compression and broadening) out of the non-linear EDFA using the 60 MHz at high powers. This may be due to this notch we observe here. Note also that the y-axes in these plots uses a log scale.

4.3.2 Towards the Supercontinuum

Despite the various mysteries of the spectra out of the non-linear amplifier, we were able to obtain better spectra out of it using another laser we had in the lab, a 60 MHz Er:fiber comb, through numerous trials with different arrangements. The switch to the 60 MHz laser was motivated by the question of whether the 100 MHz oscillator itself was the issue, convenience as the 60 MHz system was closer to the diagnostics used and the fact that we would, in general, get higher pulse energies out of the 60 MHz oscillator. As a figure for comparison, at the same peak power, pulses from the 60 MHz laser have 1.67 times the energy as pulses from the 100 MHz laser. In this section, I present progress towards obtaining dispersive waves out of the highly non-linear fiber (HNLF) for mid-IR generation. As we were concerned more with directly testing the performance of the NL-EDFA, the following tests were performed with only the NL-EDFA (see Fig. 4.14).

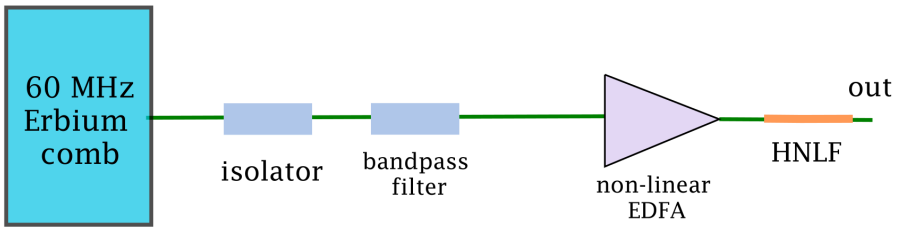

Figure 4.14: Setup used for the following tests.

Frequency-resolved optical grating (FROG) spectra shown here were recorded using sum frequency generation of the light using a BBO crystal. Using the same translation stage used to record the autocorrelations shown in Sec. 4.3.1, we vary the delay between the two input beams and record the spectrum of the second harmonic generated (SHG) with an Ocean Optics USB4000 spectrometer. This gives us the spectrum of SHG as a function of the delay between the two split beams [39]. Autocorrelations are obtained by integrating across all wavelengths for each time delay.

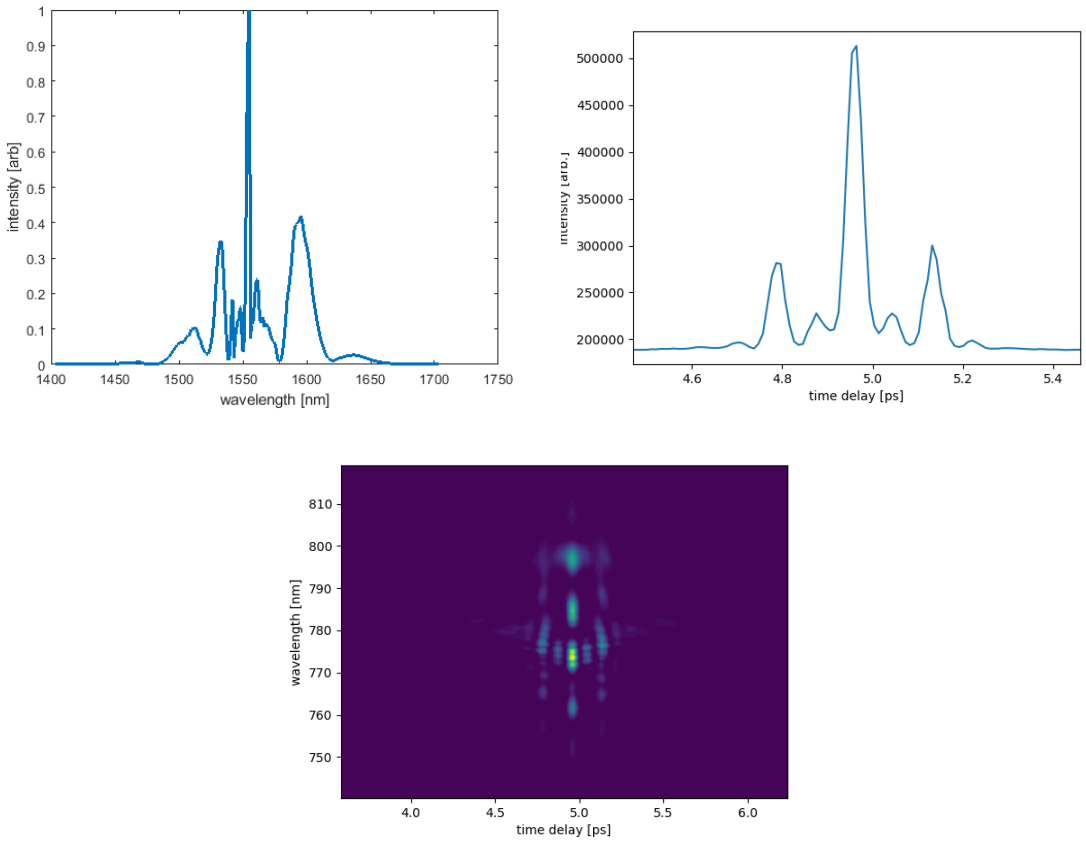

Figure 4.15: Spectrum, autocorrelation and FROG obtained with a 20 cm fiber output from the EDFA. In this case, all pumps on the EDFA were pumped at 1300 mA and the power out of the EDFA was around 312 mW. The 60 MHz comb's pre-amp current was at 850 mA. With this arrangement, we see evidence of a soliton beginning to separate from the pulse, more broadening and obtain a short pulse in the autocorrelation.

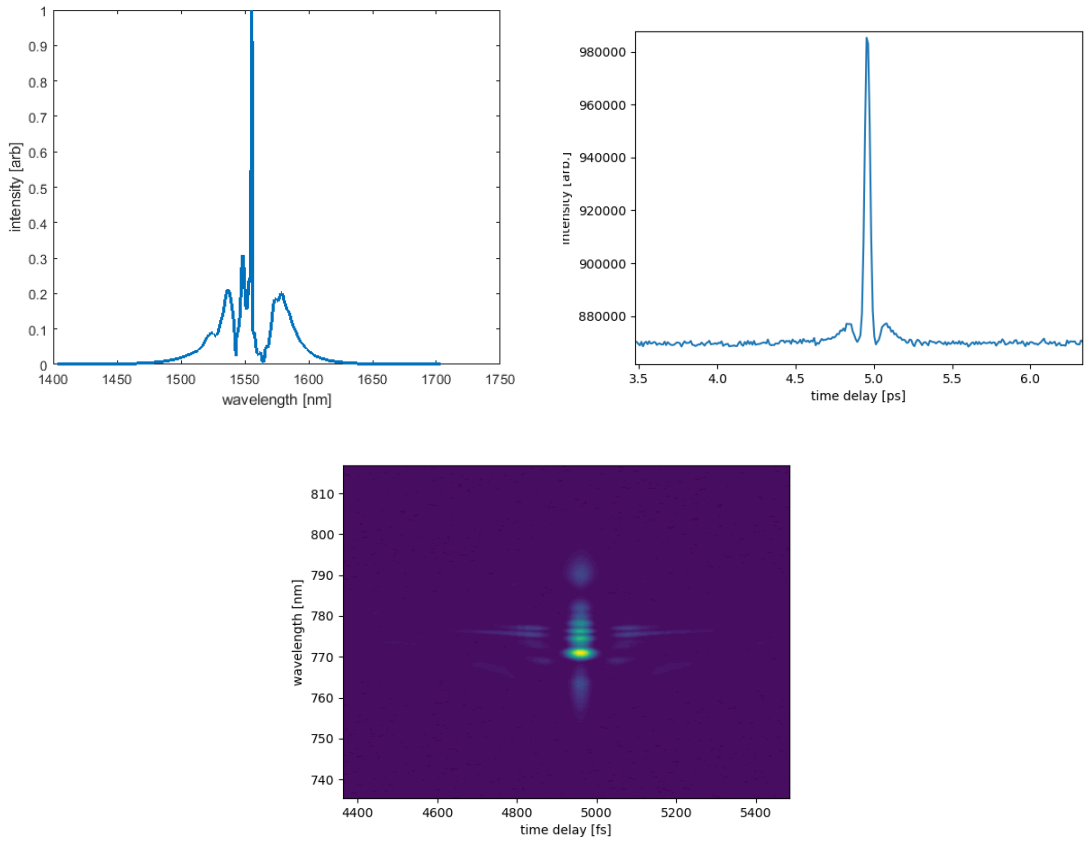

Figure 4.16: Spectrum, autocorrelation and FROG obtained with a 30 cm fiber output from the EDFA. In this case, one of the pump backwards was turned off, another was pumped with 700 mA and the pump forwards were pumped at 1200 mA. The 60 MHz comb's pre-amp current was at 850 mA. In this case, we obtain a pulse with comparable duration as that in Fig. 4.15 but pump the EDFA much less strongly. The autocorrelation here also has much less prominent sidebands. Again, we see broadening and evidence of a soliton beginning to separate from the pulse in the spectrum.

The example arrangements used to produce the pulses of Figs. 4.15 and 4.16 provide a reference of what kinds of pump and input powers may lead to the formation of a dispersive wave out of the HNLF. They suggest that the best length of fiber out of the EDFA for the particular input power used is somewhere between 20 and 30 cm.

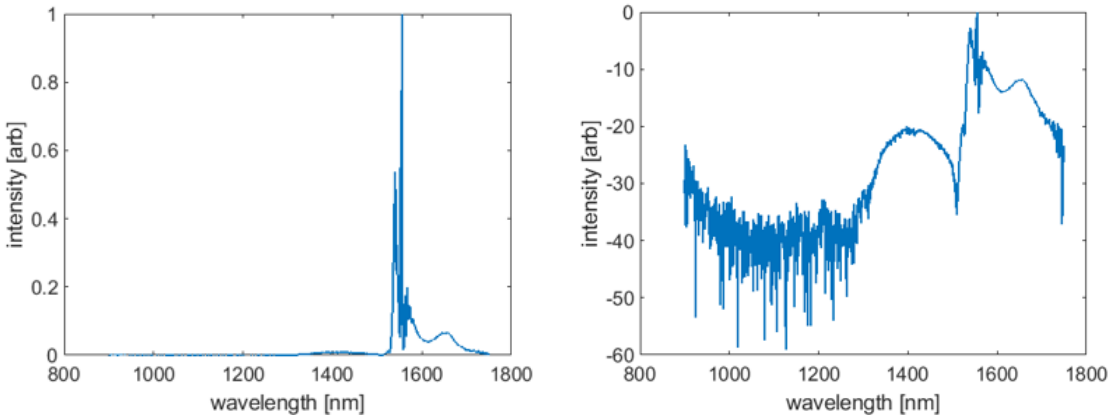

Figure 4.17: Spectra obtained from the assembly with an HNLF fiber output. The spectrum on the left is on a linear scale while the spectrum on the right is on a log scale. In this case, the fiber leading up to the HNLF is about 23 cm long and the HNLF 4 cm long. We estimate the HNLF splice loss to be < 1 dB. The pumps forward on the EDFA are pumped at 1200 mA, one backward pump is pumped at 700 mA and the last one is off. We may be seeing evidence of a dispersive wave starting to form on the blue side of this spectrum, but the efficiency of its formation is low. We were unable to achieve better efficiency with this setup.

Subsequent tests will employ these references for the HNLF assembly and to optimize dispersive wave formation.

4.3.3 Issues of Power and Spectrum

As the reader may be wondering, why are we able to obtain better broadening and pulse compression in the case used in the last section? One possible answer suggested by the results of Fig. 4.13 is that with high power out of the 60 MHz oscillator used in the last section circumvents any issues caused by a notch in the spectrum. The power used in the last section is 6.44 mW (= 107 pJ per pulse). To have the same pulse energy from the 100 MHz laser, the output power would have to be 10.73 mW. This was also a higher pulse energy/power than any shown in Fig. 4.13 so we expected the notch to be smoothed out at this power, as was the trend for higher powers in Fig. 4.13. This was confirmed through directly recording the spectrum.

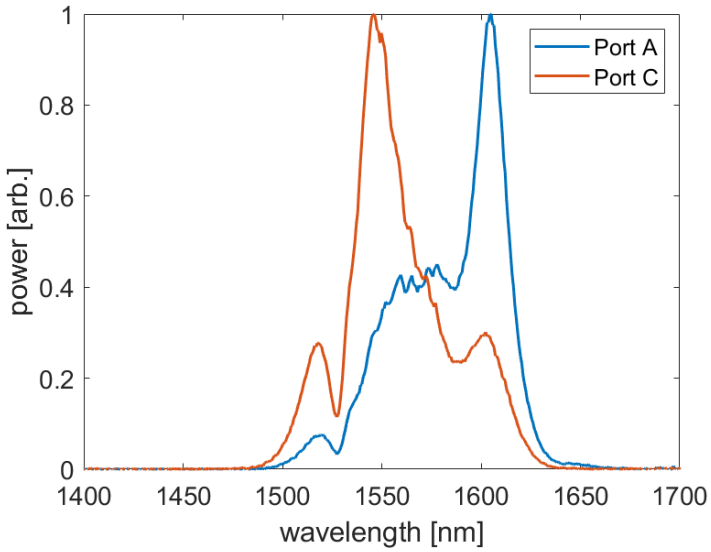

Figure 4.18: Spectra out of two different ports of the 100 MHz laser. Port C is currently in use for the CE-TAS experiment, port A was used for initial tests in this thesis. The port C spectra has more of its light centered around 1550 nm, which also explains why it outputs the highest power out of the four ports. In comparison, port A only has about 40% of its peak power at 1550. Perhaps a higher power out of the 100 MHz oscillator could change the issues observed in this work.

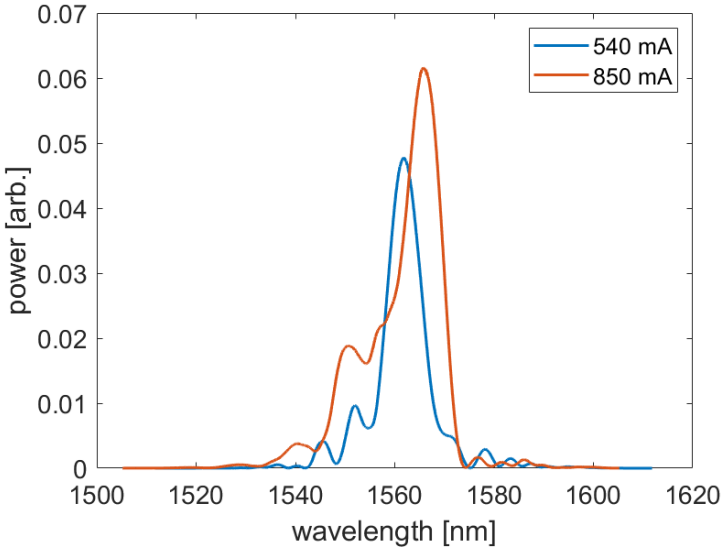

Figure 4.19: Spectra out of the port used on the 60 MHz laser (port D) at different laser pre-amplifier powers. At 540 mA, there appears to be less power at 1550 nm but this is not true at 850 mA. Perhaps this power improvement in the bandwidth of interest contributes to the better performance of the NL EDFA at 850 mA.

Figures 4.18 and 4.19 point out discrepancies between different ports of the lasers we use and

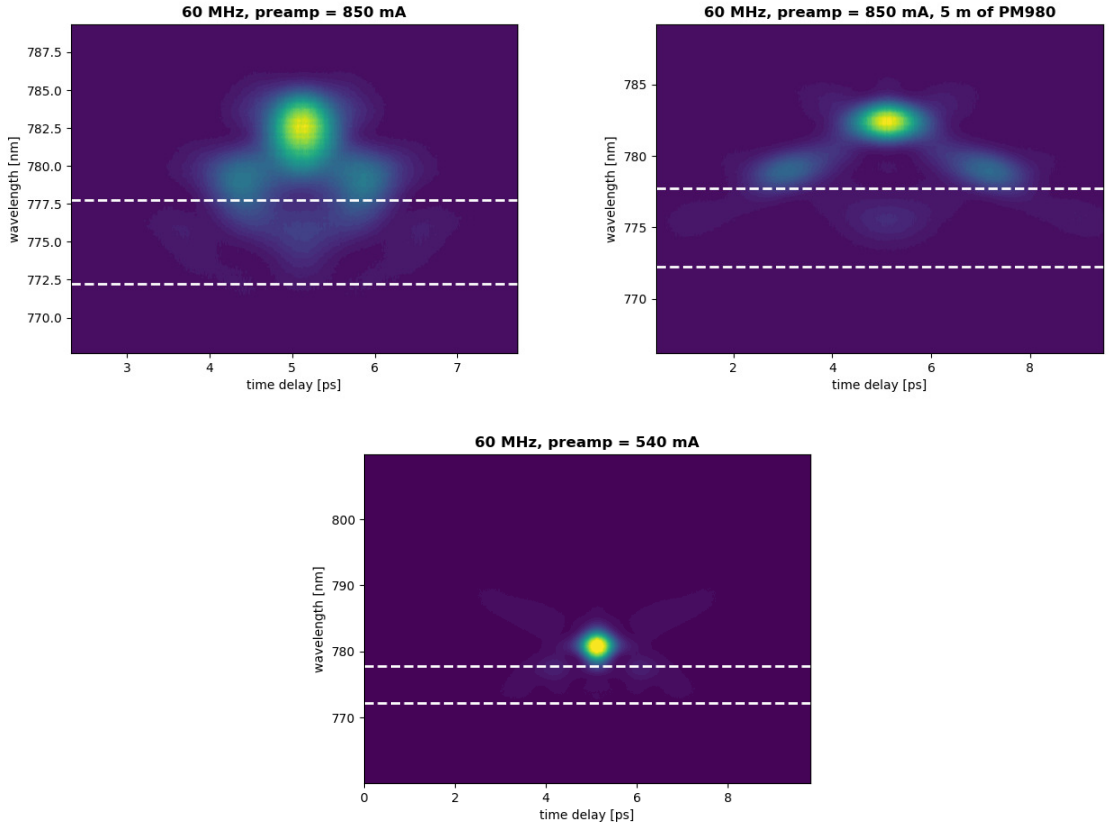

Figure 4.20: Unfiltered FROGs of the second harmonic of the 60 MHz oscillator in a few different conditions. The first figure is the output at the preamp current used in Sec. 4.3.2, the second for a case where there is 5 m of PM980 fiber after the isolator and the third at a lower preamp current which corresponded to a power output of 1.2 mW after the bandpass filter. The white dashed lines indicate the position of the bandpass filter's range. Unfortunately, the bandpass filter would, in all cases, cut off the central, highest power part of the beam and only capture the side peaks.

may indicate possible issues to investigate. Further, Fig. 4.20 clearly shows that the bandpass filter only captures a portion of the spectrum at 60 MHz, including in the cases used for the tests in this work.

It would be interesting, in this case, to test whether using port C of the 100 MHz laser and the same conditions used in Fig. 4.8 produces a better output from the EDFA. Further, would one still see the same notches in the spectrum? Perhaps similar results as those documented here could be obtained from port used (port A) of the 100 MHz laser with similar or higher pulse energies as used with the 60 MHz laser. Similarly, would the EDFA behave better with a different bandpass filter more suitably centered to the spectrum out of the 60 MHz oscillator? How much does what part of the output spectrum one captures matter?

4.3.4 Back to the 100 MHz Oscillator

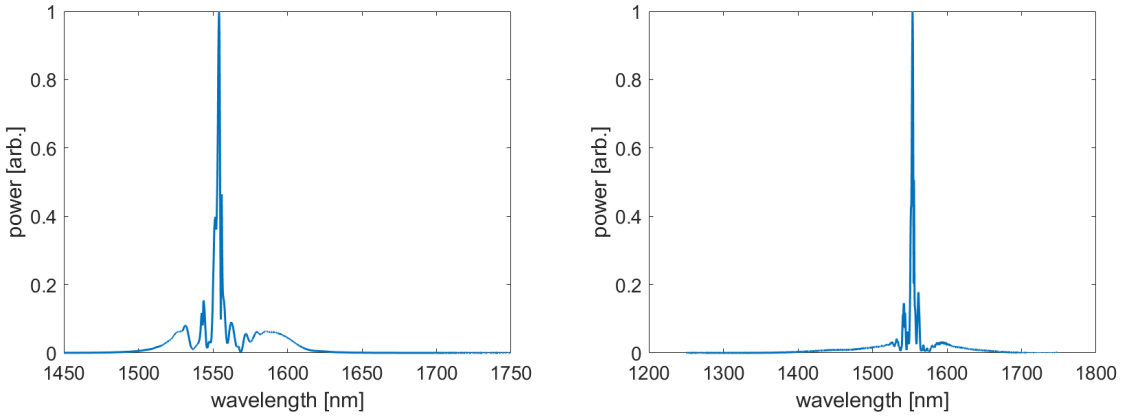

Figure 4.21: Spectra from with a 100 MHz seed, with all components of setup preceding it (including 10 m of PM980 fiber, the AOM and preamp). The figure on the left is the spectrum out of the NL EDFA, with a 30 cm fiber out. The figure on the right is after the same HNLF assembly used in Fig. 4.17. The power out of the long fiber here is 1.31 mW, which corresponds to a pulse energy of 13.1 pJ, an order of magnitude lower than the 107 pJ pulse energies used in Sec. 4.3.2 with the 60 MHz laser. All NL EDFA pumps are on their highest currents. While the spectrum out of the NL EDFA does not show as much broadening as desired, there is still some broadening. The extent of how much broadening (and what pulse durations) can be obtained in this arrangement can be further investigated.

5 Conclusion

Cavity-enhanced ultrafast spectroscopy techniques developed in our group have extended the ability to perform all-optical ultrafast spectroscopy to dilute gas-phase molecular beams and clusters. So far, our cavity-enhanced spectrometer has been used to perform transient absorption spectroscopy, and we will soon extend our work to 2D spectroscopy in the mid-IR region. Doing so will allow us to address various physical chemistry problems that arise from vibrational dynamics.

In this work, I have considered various technical details of the CE-2DIR experiment. I have carefully reviewed elements needed for one portion of the experiment and built a CAD model to implement them. In doing so, I also considered the effects of chromatic dispersion as might be relevant for the tunability of our experiment and the effect of pressure for the water clusters experiment. This model will serve as a blueprint for the experiment build and I hope the level of detail provided will prove to be useful for various build considerations/decisions.

On the fiber laser development front, I have completed much of the development needed for the signal branch. While this work may not have obtained the final desired signal spectrum from the 100 MHz laser for the OPAs, I have chronicled much of the investigations undertaken. In considering these, future work can consider what worked and what did not. Further, the results obtained using the 60 MHz laser documented here begin to answer both these questions. Simulations may also be used to guide this design [40]. The detail provided here too also points to other possible avenues of investigation. Finally, the characterization of components included in this thesis can be used for the twin signal branch build not considered here.

This thesis lays the groundwork for several design and build considerations that need to be made for the CE-2DIR experiment. This will act as a starting guide for the experimental build, while also answering many questions that might be asked regarding the experiment's needs.

References

[1] M. Maiuri, M. Garavelli, and G. Cerullo, "Ultrafast Spectroscopy: State of the Art and Open Challenges," *Journal of the American Chemical Society*, vol. 142, no. 1, p. 3–15, 2019.

[2] N. Picqué and T. W. Hänsch, "Frequency comb spectroscopy," *Nature Photonics*, vol. 13, no. 3, p. 146–157, 2019.

[3] A. Foltynowicz, P. Masłowski, A. J. Fleisher, B. J. Bjork, and J. Ye, "Cavity-enhanced optical frequency comb spectroscopy in the mid-infrared application to trace detection of hydrogen peroxide," *Applied Physics B*, vol. 110, no. 2, p. 163–175, 2012.

[4] Y. Chen, *Cavity-Enhanced Ultrafast Spectroscopy*. PhD thesis, 2018.

[5] M. A. R. Reber, Y. Chen, and T. K. Allison, "Cavity-enhanced ultrafast spectroscopy: ultrafast meets ultrasensitive," *Optica*, vol. 3, pp. 311–317, Mar 2016.

[6] M. C. Silfies, G. Kowzan, N. Lewis, and T. K. Allison, "Broadband cavity-enhanced ultrafast spectroscopy," *Physical Chemistry Chemical Physics*, vol. 23, no. 16, p. 9743–9752, 2021.

[7] Y. Chen, M. C. Silfies, G. Kowzan, J. M. Bautista, and T. K. Allison, "Tunable visible frequency combs from a Yb-fiber-laser-pumped optical parametric oscillator," *Applied Physics B*, vol. 125, no. 5, 2019.

[8] M. C. Silfies, G. Kowzan, Y. Chen, N. Lewis, R. Hou, R. Baehre, T. Gross, and T. K. Allison, "Widely tunable cavity-enhanced frequency combs," *Opt. Lett.*, vol. 45, pp. 2123–2126, Apr 2020.

[9] T. Brixner, "2D Spectroscopy." `https://www.chemie.uni-wuerzburg.de/en/ptc/labs/lehrstuhl-i-prof-t-brixner/research/2d-spectroscopy/`, Dec 2019.

[10] M. K. Petti, J. P. Lomont, M. Maj, and M. T. Zanni, "Two-dimensional spectroscopy is being used to address core scientific questions in biology and materials science," *The Journal of Physical Chemistry B*, vol. 122, no. 6, p. 1771–1780, 2018.

[11] D. J. Nesbitt and R. W. Field, "Vibrational energy flow in highly excited molecules:nbsp; role of intramolecular vibrational redistribution," *The Journal of Physical Chemistry*, vol. 100, no. 31, p. 12735–12756, 1996.

[12] H. S. Frank and W.-Y. Wen, "Ion-solvent interaction. structural aspects of ion-solvent interaction in aqueous solutions: a suggested picture of water structure," *Discuss. Faraday Soc.*, vol. 24, pp. 133–140, 1957.

[13] D. L. Maser, G. Ycas, W. I. Depetri, F. C. Cruz, and S. A. Diddams, "Coherent frequency combs for spectroscopy across the 3–5 µm region," *Applied Physics B*, vol. 123, no. 5, 2017.

[14] R. W. Boyd, *Nonlinear Optics*. Academic Press, 2007.

[15] G. P. Agrawal, *Nonlinear Fiber Optics*. Academic Press, 2019.

[16] A. Sell, G. Krauss, R. Scheu, R. Huber, and A. Leitenstorfer, "8-fs pulses from a compact Er:fiber system: quantitative modeling and experimental implementation," *Opt. Express*, vol. 17, pp. 1070–1077, Jan 2009.

[17] T. K. Allison, "Cavity-enhanced ultrafast two-dimensional spectroscopy using higher order modes," *Journal of Physics B: Atomic, Molecular and Optical Physics*, vol. 50, no. 4, 2017.

[18] A. Catanese, J. Rutledge, M. C. Silfies, X. Li, H. Timmers, A. S. Kowligy, A. Lind, S. A. Diddams, and T. K. Allison, "Mid-infrared frequency comb with 6.7 w average power based on difference frequency generation," *Opt. Lett.*, vol. 45, pp. 1248–1251, Mar 2020.

[19] "HC Photonics - PPLN Guide-Materials." `https://www.hcphotonics.com/ppln-guide-materials`.

[20] G. Arisholm, R. Paschotta, and T. Südmeyer, "Limits to the power scalability of high-gain optical parametric amplifiers," *J. Opt. Soc. Am. B*, vol. 21, pp. 578–590, Mar 2004.

[21] "Gaussian Beam Optics, CVI Melles Griot 2009 Technical Guide." `http://experimentationlab.berkeley.edu/sites/default/files/MOT/Gaussian-Beam-Optics.pdf`, 2009.

[22] W. Nagourney, *Quantum Electronics for Atomic Physics*. Oxford Univ. Press, 2010.

[23] Optical Fiber Solutions (OFS), "HNLF-PM." https://fiber-optic-catalog.ofsoptics.com/HNLF-PM-1159.

[24] I. H. Malitson, "Interspecimen comparison of the refractive index of fused silica," *J. Opt. Soc. Am.*, vol. 55, pp. 1205–1209, Oct 1965.

[25] E. Hecht, *Optics, 2nd ed.* Addison Wesley, 1987.

[26] P. Hamm and M. Zanni, *Concepts and Methods of 2D Infrared Spectroscopy.* Cambridge University Press, 2011.

[27] Optique Ingenieur, "Hermite-gaussian modes." http://www.optique-ingenieur.org/en/courses/OPI_ang_M01_C03/co/Contenu_13.html.

[28] Isomet Corporation, "Acousto-optic modulation." http://www.isomet.com/App-Manual_pdf/AO%20Modulation.pdf.

[29] J. B. Paul, C. P. Collier, R. J. Saykally, J. J. Scherer, and A. O'Keefe, "Direct measurement of water cluster concentrations by infrared cavity ringdown laser absorption spectroscopy," *The Journal of Physical Chemistry A*, vol. 101, no. 29, p. 5211–5214, 1997.

[30] C. Hill, "The HITRAN Database." https://hitran.org/.

[31] P. F. Bernath, *Spectra of Atoms and Molecules.* Oxford Univ. Press, 2020.

[32] C. Hill, "Definitions and units: Line-by-line parameters." https://hitran.org/docs/definitions-and-units/.

[33] W. Demtröder, *Laser Spectroscopy: Basic Concepts and Instrumentation.* Springer, 2003.

[34] F. Schreier, "The voigt and complex error function: A comparison of computational methods," *Journal of Quantitative Spectroscopy and Radiative Transfer*, vol. 48, no. 5, pp. 743–762, 1992. Special Issue Conference on Molecular Spectroscopic Databases.

[35] U. van Burck, D. P. Siddons, J. B. Hastings, U. Bergmann, and R. Hollatz, "Nuclear forward scattering of synchrotron radiation," *Phys. Rev. B*, vol. 46, pp. 6207–6211, 1992.

[36] Y. Kagan, A. M. Afanas'ev, and V. G. Kohn, "On excitation of isomeric nuclear states in a crystal by synchrotron radiation," *Journal of Physics C: Solid State Physics*, vol. 12, pp. 615–631, Feb 1979.

[37] A. M. Weiner, *Ultrafast Optics*. Wiley, 2009.

[38] Thorlabs, Inc., "Polarization-Maintaining Single Mode Optical Fiber." `https://www.thorlabs.com/newgrouppage9.cfm?objectgroup_id=1596&pn=PM980-XP`.

[39] D. Kane and R. Trebino, "Characterization of arbitrary femtosecond pulses using frequency-resolved optical gating," *IEEE Journal of Quantum Electronics*, vol. 29, no. 2, pp. 571–579, 1993.

[40] G. Ycas, *Laser Frequency Combs for Precision Astronomical Spectroscopy*. PhD thesis, 2013.